Microglia mediate synaptic plasticity induced by 10 Hz repetitive transcranial magnetic stimulation

Amelie Eichler[1], Dimitrios Kleidonas[1,2,3], Zsolt Turi[1], Maximilian Fliegauf[4,5], Matthias Kirsch[1], Dietmar Pfeifer[6], Takahiro Masuda[4,7], Marco Prinz[4,8,9], Maximilian Lenz[1,#], Andreas Vlachos[1,9,10;#]

[1]Department of Neuroanatomy, Institute of Anatomy and Cell Biology, Faculty of Medicine, University of Freiburg, Freiburg, Germany.

[2]Spemann Graduate School of Biology and Medicine, University of Freiburg, Freiburg, Germany.

[3]Faculty of Biology, University of Freiburg, Freiburg, Germany.

[4]Institute of Neuropathology, Faculty of Medicine, University of Freiburg, Freiburg, Germany.

[5]Department of Pharmaceutical Biology and Biotechnology, Institute of Pharmaceutical Sciences, University of Freiburg, Freiburg, Germany.

[6]Department of Hematology, Oncology and Stem Cell Transplantation, Medical Center, Faculty of Medicine, University of Freiburg, Freiburg, Germany.

[7]Department of Molecular and System Pharmacology, Graduate School of Pharmaceutical Sciences, Kyushu University, Fukuoka 812-8582, Japan.

[8]Signalling Research Centres BIOSS and CIBSS, University of Freiburg, Freiburg, Germany.

[9]Center for Basics in Neuromodulation (NeuroModulBasics), Faculty of Medicine, University of Freiburg, Freiburg, Germany.

[10]Center Brain Links Brain Tools, University of Freiburg, Freiburg, Germany.

[#] joint senior authors

*Correspondence to: Andreas Vlachos, M.D.
Department of Neuroanatomy
Institute of Anatomy and Cell Biology
Albert-Ludwigs-Universität Freiburg
Albertstr. 17
79104 Freiburg, Germany
Email: andreas.vlachos@anat.uni-freiburg.de

ABSTRACT

Microglia—the resident immune cells of the central nervous system—sense the activity of neurons and regulate physiological brain functions. They have been implicated in the pathology of brain diseases associated with alterations in neural excitability and plasticity. However, experimental and therapeutic approaches that modulate microglia function in a brain-region-specific manner have not been established. In this study, we tested for the effects of repetitive transcranial magnetic stimulation (rTMS), a clinically employed non-invasive brain stimulation technique, on microglia-mediated synaptic plasticity. 10 Hz electromagnetic stimulation triggered a release of plasticity-promoting cytokines from the microglia in organotypic brain tissue cultures, while no changes in microglial morphology or microglia dynamics were observed. Indeed, substitution of tumor necrosis factor alpha (TNFα) and interleukin 6 (IL6) preserved synaptic plasticity induced by 10 Hz stimulation in the absence of microglia. Consistent with these findings, *in vivo* depletion of microglia abolished rTMS-induced changes in neurotransmission in the medial prefrontal cortex (mPFC) of anesthetized mice. We conclude that rTMS affects neural excitability and plasticity by modulating the release of cytokines from microglia.

Keywords: Microglia, rTMS, microglia depletion, excitatory synaptic plasticity, TNFα

46 **INTRODUCTION**

47 Despite its increasingly prevalent clinical use, e.g., for the treatment of patients with pharmaco-
48 resistant depression, the cellular and molecular effects of repetitive transcranial magnetic
49 stimulation (rTMS) remain poorly understood (Cirillo et al., 2017; Muller-Dahlhaus and
50 Vlachos, 2013). It is widely known however, that the electric fields produced by non-invasive
51 magnetic brain stimulation modulate neural excitability and synaptic transmission in cortical
52 circuits (Pell et al., 2011). These changes require neural activity, i.e., action potential induction,
53 and Ca^{2+}-dependent signaling pathways, i.e., NMDA receptors and L-Type voltage-gated
54 calcium channels (Lenz et al., 2015). Such changes are consistent with the long-term
55 potentiation (LTP) of synaptic neurotransmission (Vlachos et al., 2012). It remains unclear
56 however, how rTMS and the induction of "LTP-like" plasticity asserts positive effects in
57 clinical settings.

58 Recent work suggests that microglia, the resident immune cells of the brain, sense and
59 regulate synaptic transmission and plasticity (Badimon et al., 2020; Schafer et al., 2012). There
60 is evidence that changes in network activity modulate microglia states (Pfeiffer et al., 2016;
61 Stowell et al., 2019). These changes are reflected by the dynamic extension and retraction of
62 microglial processes, by the formation of physical contacts between microglia and neurons,
63 and by the activity-dependent secretion of plasticity-modulating factors (Akiyoshi et al., 2018;
64 Cserep et al., 2020; Sheppard et al., 2019). Specifically, the plasticity-modulating effects of
65 pro-inflammatory cytokines, such as tumor necrosis factor alpha (TNFα) and interleukin 6
66 (IL6), have been demonstrated in several experimental settings, both *in vitro* and *in vivo* (Heir
67 and Stellwagen, 2020; Santello et al., 2011; Stellwagen and Malenka, 2006). These findings
68 suggest that microglia play an important role in neural function and plasticity. Considering
69 their role in pathological brain states (Graeber and Streit, 2010; Prinz et al., 2019; Prinz et al.,
70 2021), it is interesting to theorize that the therapeutic effects of rTMS could—at least in part—

71 depend on the modulation of microglia function. Indeed, evidence has been provided that rTMS
72 affects microglial markers (Clarke et al., 2017; Cullen and Young, 2016; Li et al., 2021; Muri
73 et al., 2020; Stevanovic et al., 2019). However, direct experimental evidence determining the
74 role of microglia in rTMS-induced neural plasticity is currently not available.

75 To address the biological relevance of microglia in rTMS-induced synaptic plasticity,
76 we depleted microglia from organotypic brain tissue cultures and the adult mouse brain and
77 probed synaptic plasticity with a 10 Hz stimulation protocol. In turn, we tested for the effects
78 of 10 Hz magnetic stimulation on the structural and functional properties of microglia and
79 employed *in vitro* cytokine release assays to identify the plasticity promoting effects of
80 microglial factors secreted after rTMS.

81 **MATERIALS AND METHODS**

82 **Ethics statement.** Mice were maintained in a 12 h light/dark cycle with food and water
83 available *ad libitum*. Every effort was made to minimize distress and pain of animals. All
84 experimental procedures were performed according to German animal welfare legislation and
85 approved by the competent authority (Regierungspräsidium Freiburg, G-20/154) appropriate
86 animal welfare committee and the animal welfare officer of Albert-Ludwigs-University
87 Freiburg, Faculty of Medicine (X-17/07K, X-17/09C, X-18/02C).

88 **Preparation of tissue cultures.** Entorhino-hippocampal tissue cultures were prepared at
89 postnatal day 3-5 from *C57BL/6J*, *HexB-tdTom* (Masuda et al., 2020), and *C57BL/6-Tg(TNFa-*
90 *eGFP)* (Lenz et al., 2020) mice of either sex as previously described (Lenz et al., 2015).
91 Cultivation medium contained 50% (v/v) MEM, 25% (v/v) basal medium eagle, 25% (v/v)
92 heat-inactivated normal horse serum, 25 mM HEPES buffer solution, 0.15% (w/v) bicarbonate,
93 0.65% (w/v) glucose, 0.1 mg/ml streptomycin, 100 U/ml penicillin, and 2 mM glutamax. The
94 pH was adjusted to 7.3. All tissue cultures were allowed to mature for at least 18 days in a
95 humidified atmosphere with 5% CO_2 at 35°C. Cultivation medium was replaced 3 times per
96 week.

97 **Microglia depletion *in vitro* and *in vivo*.** Tissue cultures were treated immediately after
98 preparation (div 0) with the CSF-1R inhibitor PLX3397 (50 nM; #2501 Axon) for at least 18
99 days. Vehicle-only treated cultures (DMSO, 0.1 µl) served as age- and time-matched controls.
100 For *in vivo* microglia depletion, we used the CSF-1R inhibitor BLZ945 (kindly provided by
101 Novartis, Basel, Switzerland) dissolved in 20% (2-hydroxypropyl)-β-cyclodextrin (Sigma-
102 Aldrich, Germany). A dose of 200 mg/kg bodyweight was applied by oral gavage in adult (8-
103 weeks old) mice for 7 consecutive days as previously described (Hagemeyer et al., 2017;

104 Masuda et al., 2020). No weight loss or any apparent signs of stress could be detected
105 throughout the treatment period.

106 **Repetitive magnetic stimulation *in vitro*.** Tissue cultures (≥ 18 days *in vitro*) were transferred
107 to a 35 mm Petri Dish filled with pre-warmed standard extracellular solution containing (in
108 mM): 129 NaCl, 4 KCl, 1 $MgCl_2$, 2 $CaCl_2$, 4.2 glucose, 10 HEPES, 0.1 mg/ml streptomycin,
109 100 U/ml penicillin, pH 7.4 adjusted with NaOH, osmolarity adjusted with sucrose to 380-390
110 mOsm. Cultures were stimulated using the Magstim Rapid^2 stimulator (Magstim Company,
111 UK) connected to a Double AirFilm® Coil (coil parameters according to manufacturer's
112 description: average inductance = 12 µH; pulse rise time approximately 80 µs; pulse duration
113 = 0.5 ms, biphasic; Magstim Company, UK) with a biphasic current waveform. Cultures were
114 positioned approximately 1 cm under the center of the coil and oriented in a way that the
115 induced electric field was parallel to the dendritic tree of CA1 pyramidal neurons. The
116 stimulation protocol consisted of 900 pulses at 10 Hz (50% maximum stimulator output).
117 Cultures were kept in the incubator for at least 2 h after stimulation before experimental
118 assessment. Age- and time-matched control cultures were not stimulated, but otherwise treated
119 identical to stimulated cultures (sham stimulation). For cytokine substitution experiments
120 TNFα (5 ng/ml; #410-MT RD Systems) and IL6 (2.5 ng/ml; #406-ML RD Systems) were
121 added to the stimulation medium.

122 **Repetitive magnetic stimulation *in vivo*.** rTMS was carried out in adult (~8 weeks old)
123 urethane-anesthetized (1.25 $g\,kg^{-1}$, intraperitoneal; 0.125 $g\,kg^{-1}$, subcutaneous) *C57BL/6J*
124 mice of either sex. The head was placed under the coil with the medial prefrontal cortex
125 (mPFC) under the center. During the stimulation, the brain-to-coil distance was kept minimal,
126 while brain-to-coil contact was avoided. Repetitive stimulation was performed at fixed
127 intensities of 60% MSO (which corresponds to 90% motor threshold, see (Lenz et al., 2016))

128 using the same 10-Hz stimulation protocol described above. Control animals placed near the
129 coil during stimulation were not stimulated but otherwise treated identically. All animals were
130 transferred back to their cages with appropriate body temperature control and were held in
131 anesthesia for 2 h under continuous surveillance. After the waiting period, ketamine/xylazin
132 (100 mg kg^{-1} / 20 mg kg^{-1}; i.p. application) was injected to achieve a suitable analgesia before
133 rapid decapitation.

134 The brain was prepared as previously described (Lenz et al., 2021; Ting et al., 2018).
135 After dissection, the brain was embedded in low-melting agar (1.8% w/v in PBS; Sigma
136 Aldrich #A9517) and frontal sections (350 µm thickness) containing the mPFC were prepared
137 using a Leica VT1200S vibratome with a cutting angle of 15°. The brain was cut in NMDG-
138 aCSF [containing (in mM) 92 NMDG, 2.5 KCl, 1.25 NaH_2PO_4, 30 $NaHCO_3$, 20 HEPES, 25
139 glucose, 2 thiourea, 5 Na-ascorbate, 3 Na-pyruvate, 0.5 $CaCl_2$, and 10 $MgSO_4$, (pH = 7.3–7.4)]
140 at approximately 0°C. After cutting slices were recovered in NMDG-aCSF at 34°C. Sodium
141 spike-in was performed according to a previously established protocol that is suitable for ~8
142 week old animals (Lenz et al., 2021; Ting et al., 2018). After recovery, we transferred the slices
143 to a holding chamber [holding-aCSF; containing (in mM) 92 NaCl, 2.5 KCl, 1.25 NaH_2PO_4,
144 30 $NaHCO_3$, 20 HEPES, 25 glucose, 2 thiourea, 5 Na-ascorbate, 3 Na-pyruvate, 2 $CaCl_2$, and
145 2 $MgSO_4$, (pH = 7.3–7.4)] at room temperature in which slices were maintained at least half an
146 hour until electrophysiological assessment.

147 **Propidium iodide staining.** Tissue cultures were incubated with propidium iodide (PI, 5
148 µg/ml; #P3566 Invitrogen) for 2 h, washed in phosphate buffered saline (PBS) and fixed as
149 described below. Cultures treated for 4 h with NMDA (50 µg/ml; #0114 Tocris) served as
150 positive controls in these experiments. Cell nuclei were stained with DAPI, sections were
151 mounted on microscope slides and confocal images were acquired as described below.

152 **Immunostaining and imaging.** Tissue cultures were fixed overnight in a solution of 4% (w/v)
153 paraformaldehyde (PFA) in PBS (prepared from 16% PFA stocks in phosphate buffered saline
154 according to manufacturer's instruction; #28908 Thermo Scientific). After fixation, cultures
155 were washed in PBS (0.1 M, pH 7.4) and consecutively incubated for 1 h with 10% (v/v) normal
156 goat serum (NGS) in 0.5% (v/v) Triton X-100 containing PBS to reduce nonspecific staining
157 and to increase antibody penetration. Subsequently, cultures were incubated overnight at 4°C
158 with rabbit anti-Iba1 (1:1000; #019-19741 Fujifilm Wako) in PBS with 10% NGS and 0.1%
159 Triton X-100. Sections were washed and incubated overnight at 4°C with appropriate Alexa
160 Fluor® dye-conjugated secondary antibodies (1:1000, donkey anti-rabbit Alexa Fluor 488 or
161 647; #A-21206 or #A-32795 Invitrogen) in PBS with 10% NGS or NHS, 0.1% Triton X-100.
162 For post-hoc visualization of patched pyramidal cells, Streptavidin Alexa Fluor 488 or 633
163 (Streptavidin A488, 1:1000; #S32354 Invitrogen; Streptavidin A633, 1:1000; #S21375
164 Invitrogen) was added to the secondary antibody incubation solution. DAPI nuclear stain
165 (1:2000 in PBS for 20 minutes; #62248 Thermo Scientific) was used to visualize
166 cytoarchitecture. Cultures were washed, transferred onto glass slides and mounted for
167 visualization with DAKO anti-fading mounting medium (#S302380-2 Agilent).

168 A Leica SP8 laser-scanning microscope equipped with a 20x multi-immersion (NA
169 0.75; Leica), a 40x oil-immersion (NA 1.30; Leica) and a 63x oil-immersion objective (NA
170 1.40; Leica) was used for confocal image acquisition. Images for analysis of microglia cell
171 density (Figure 1) and images of propidium iodide stainings (Figure 3) were acquired with a
172 20x objective at 0.75x optical zoom (resolution: 512 x 512 px). Image stacks for spine density
173 and spine volume analysis (Figure 6) were acquired with a 63x oil-immersion objective at 5.0x
174 optical zoom (resolution: 1024 x 1024, $\Delta z = 0.22$ µm at ideal Nyquist rate). Image stacks of
175 Iba1 stained *HexB-tdTom* cultures (Figure S1) were acquired with a 20x objective at 2.0x
176 optical zoom (resolution: 512 x 512 px). Image stacks of Iba1 stained acute cortical slices

177 (Figure 11) were acquired using a 40x oil-immersion objective at 2.0x optical zoom (resolution
178 1024x1024, $\Delta z = 1$ µm). Laser intensity and detector gain were set to achieve comparable
179 overall fluorescence intensity throughout stacks between all groups in each experimental
180 setting.

181 **Live-cell imaging.** Live-cell imaging of tissue cultures was performed at a Zeiss LSM800
182 microscope equipped with a 10x water-immersion (NA 0.3; Carl Zeiss) and a 40x water-
183 immersion objective (NA 1.0; Carl Zeiss). Filter membranes with 2 to 6 cultures were placed
184 in a 35 mm Petri Dish containing pre-oxygenated imaging solution consisting of 50% (v/v)
185 MEM, 25% (v/v) basal medium eagle, 50 mM HEPES buffer solution (25% v/v), 0.65% (w/v)
186 glucose, 0.15% (w/v) bicarbonate, 0.1 mg/ml streptomycin, 100 U/ml penicillin, 2 mM
187 glutamax and 0.1 mM trolox. The cultures were kept at 35°C during the imaging procedure.

188 Live-cell imaging of homozygous (*HexB*$^{tdT/tdT}$) and heterozygous (*HexB*$^{tdT/+}$) cultures
189 prepared from *HexB-tdTom* transgenic animals was performed to assess microglia morphology
190 after rMS. Cultures were stimulated as described above (rMS and sham stimulation) and
191 imaging was started immediately in imaging solution under continuous oxygenation (5% CO_2
192 / 95% O_2). For 3 hours, every 2 minutes a z-stack of the same cell was recorded using a 40x
193 water-immersion objective with $\Delta z = 1$ µm at ideal Nyquist rate and an optical zoom of 1.0x
194 (resolution 512 x 512 px, 2x line average). Laser intensity and detector gain were initially set
195 and were kept constant over image acquisition time.

196 Live-cell imaging of *C57BL/6-Tg(TNFa-eGFP)* cultures was performed to monitor
197 TNFα expression after rMS as an indicator of neuroinflammation. Cultures were stimulated as
198 described above (rMS and sham stimulation) and kept in the incubator after stimulation. After
199 3 hours a z-stack of each culture was recorded using a 10x water-immersion objective with Δz
200 = 6.3 µm at ideal Nyquist rate and an optical zoom of 0.5x (resolution 1024 x 1024 px). Laser

201 intensity and detector gain were initially set to keep the fluorescent signal in a dynamic range
202 throughout the experiment and were kept constant.

203 Confocal image stacks were stored as .czi files.

204 **Transcriptome Microarray.** Tissue cultures that were cultivated on one filter membrane (3
205 cultures) were transferred as one sample into RLT buffer (QIAGEN) and RNA was isolated
206 according to the manufacturer's instructions (RNeasy Plus Micro Kit; #74034 QIAGEN). RNA
207 was eluted in 50 µl water and precipitated in 0.75 M ammonium-acetate and 10 µg glycogen
208 (#R0551 Thermo Scientific) by adding 125 µl ethanol (100%). Samples were incubated at -
209 80°C overnight and consecutively centrifuged for 30 minutes at 4°C. Pellets were washed with
210 70% ethanol, centrifuged again and dried. Finally, pellets were dissolved in water for further
211 processing. RNA concentration and integrity was consecutively analyzed by capillary
212 electrophoresis using a Fragment Analyser (Advanced Analytical Technologies, Inc., USA).
213 RNA samples with RNA quality numbers (RQN) > 8.0 were further processed with the
214 Affymetrix WT Plus kit and hybridized to Clariom S mouse arrays as described by the
215 manufacturer (Thermo Fisher, Germany). Briefly, labeled fragments were hybridized to arrays
216 for 16 h at 45°C, 60 rpm in a GeneChip™ Hybridization Oven (Thermo Fisher, Germany).
217 After washing and staining, the arrays were scanned with the Affymetrix GeneChip Scanner
218 3000 7G (Thermo Fisher, Germany). CEL files were produced from the raw data with
219 Affymetrix GeneChip Command Console Software Version 4.1.2 (Thermo Fisher, Germany).

220 **Cytokine detection assay.** To analyze protein release upon rMS, cultures were stimulated on
221 incubation medium in interface configuration with three cultures grown on one filter
222 membrane. Three hours after stimulation, both incubation medium (for detection of protein
223 release) and tissue cultures (for gene expression analysis) were collected and frozen in liquid
224 nitrogen until further processing.

225 For cytokine detection, a V-Plex Proinflammatory Panel 1 (mouse) Kit Plus
226 (#K15048G Mesoscale Discovery) was used. The collected incubation medium was diluted 1:1
227 in diluent provided with the kit. Protein detection was performed according to the
228 manufacturer's instructions. A pre-coated plate with capture antibodies on defined spots was
229 incubated with the diluted samples overnight. After washing, samples were incubated for over
230 night with a solution containing electrochemiluminescent MSD SULFO-TAG detection
231 antibodies (Mesoscale Discovery; Antibodies: Anti-ms TNFα Antibody #D22QW, Anti-ms
232 IL6 Antibody #D22QX, Anti-ms CXCL1 Antibody #D22QT). After washing, samples were
233 measured with a MESO QuickPlex SQ 120 instrument (Mesoscale Discovery). The respective
234 protein concentrations were determined using the MSD DISCOVERY WORKBENCH
235 software (Mesoscale Discovery).

236 **RNA Isolation and Quantitative reverse transcription PCR (RT-qPCR).** RNA isolation
237 for qPCR analysis was performed as follows. Tissue cultures that were cultivated on one filter
238 membrane (3 cultures) were transferred as one sample into RNA Protection buffer (New
239 England Biolabs) and RNA was isolated according to the manufacturer's instructions
240 (Monarch® Total RNA Miniprep Kit; #T2010S New England Biolabs). As a quality control,
241 the RIN (RNA integrity number) value of RNA isolated from tissue culture was determined
242 using the Agilent RNA 6000 Pico Kit (#5067-1513 Agilent) with a 2100 Bioanalyzer
243 (#G2939BA Agilent; Mean RIN value: 8.9). Purified RNA was consecutively reverse
244 transcribed (RevertAid RT Kit; #K1691 Thermo Scientific). cDNA was diluted in water to a
245 final concentration of 3 ng/ml. RT-qPCR was performed using a C1000 Touch Thermal Cycler
246 (BIO-RAD) and the CFX 384 Real-Time PCR system (BIO-RAD). 13.5 ng target cDNA
247 diluted in TaqMan Gene Expression Master Mix (#4369016 Applied Biosystems) were
248 amplified using standard TaqMan gene expression assays (Applied Biosystems; Assay-IDs:
249 *Gapdh*: Mm99999915_g1; *Tnf*: Mm00443258_m1; *Il6*: Mm00446190_m1; *Cxcl1*:

250 Mm04207460_m1). The RT-qPCR protocol was performed as follows: 1 cycle of 50°C for 2
251 min, 1 cycle of 95°C for 10 min, 40 cycles of 95°C for 15 s and 60°C for 1 min. Of each sample
252 three technical replicates were used and no amplification was detected in non-template
253 controls. Amplification curves were excluded from further analysis if efficiency values were
254 less than 90 or exceeded 110 according to automated calculation by the Bio-Rad CFX Maestro
255 software package. Data were exported and stored on a computer as .pcrd-files.

256 **Whole-cell patch-clamp recordings.** Whole-cell patch-clamp recordings were carried out at
257 35°C (3-6 neurons per culture). Patch pipettes contained (in mM) 126 K-gluconate, 10 HEPES,
258 4 KCl, 4 ATP-Mg, 0.3 GTP-Na_2, 10 PO-Creatine, 0.3% (w/v) biocytin (pH 7.25 with KOH,
259 290 mOsm with sucrose), having a tip resistance of 4-6 MΩ. Pyramidal neurons were visually
260 identified using a LN-Scope (Luigs & Neumann) equipped with an infrared dot-contrast and a
261 40x water-immersion objective (NA 0.8; Olympus). Electrophysiological signals were
262 amplified using a Multiclamp 700B amplifier, digitized with a Digidata 1550B digitizer, and
263 visualized with the pClamp 11 software package.

264 For whole-cell patch-clamp recordings of CA1 pyramidal neurons in tissue cultures,
265 the bath solution contained (in mM) 126 NaCl, 2.5 KCl, 26 $NaHCO_3$, 1.25 NaH_2PO_4, 2 $CaCl_2$,
266 2 $MgCl_2$, and 10 glucose (aCSF) and was oxygenated continuously (5% CO_2 / 95% O_2).
267 Spontaneous excitatory postsynaptic currents (sEPSCs) of CA1 pyramidal neurons were
268 recorded in voltage-clamp mode at a holding potential of -60 mV. Series resistance was
269 monitored before and after each recording and recordings were discarded if the series resistance
270 reached ≥ 30 MΩ. For mEPSC recordings of CA1 pyramidal neurons, D-APV (10 µM;
271 #ab120003 Abcam), (-)-Bicuculline-Methiodide (10 µM; #ab120108 Abcam) and TTX (0.5
272 µM; #18660-81-6 Biotrend) were added to the external solution.

Whole-cell patch-clamp recordings of superficial (layer 2/3) cortical pyramidal neurons in acute mouse brain slices were carried out in a bath solution containing holding-aCSF. For sEPSC recordings, layer 2/3 pyramidal neurons were held at -70 mV in voltage-clamp mode.

For recording of intrinsic cellular properties in current-clamp mode, pipette capacitance of 2.0 pF was corrected and series resistance was compensated using the automated bridge balance tool of the MultiClamp commander. I-V-curves were generated by injecting 1 s square pulse currents starting at -100 pA and increasing in 10 pA steps (sweep duration: 2 s). Series resistance was monitored, and recordings were discarded if the series resistance reached ≥ 30 MΩ.

Multi-scale modeling. A 3-dimensional mesh model was created with two compartments, i.e., bath solution and organotypic tissue culture, using the finite element method and the program Gmsh (4.8.4). Local mesh resolution was increased from 0.01 to 0.004 units in the CA1 region of the culture, i.e., region of interest (ROI), where neurons were placed. The final mesh consisted of 3.55×10^6 nodes and 2.11×10^7 tetrahedrons. The mean tetrahedron edge length was 5.6 µm in the ROI. The physical dimensions of the mesh model were adapted from the *in vitro* setting.

The coil-to-culture distance was kept at 10 mm and the coil was positioned above the culture. Electrical conductivities for the bath and culture were 1.654 S m^{-1} and 0.275 S m^{-1}, respectively. The rate of change of the coil current was set to 1.4 A μs^{-1} at 1% MSO and it was scaled up to 50% MSO. Macroscopic electric field simulations were performed using SimNIBS (3.2.4) and Matlab (2020b). A validated 70 mm MagStim figure-of-eight coil was used in all simulations.

For multi-scale modeling, we used the Neuron Modeling for TMS (NeMo-TMS) framework to study the biological responses of CA1 pyramidal neurons to biphasic single pulse

297 TMS and rTMS (Shirinpour et al., 2021). Axonal morphology was adopted from an example
298 cell (Shirinpour et al., 2021). For all neurons, we implemented the generalized version of the
299 Jarsky model (Shirinpour et al., 2021).

300 We extracted the membrane potentials and voltage-gated calcium 'influx' from the
301 somatic and dendritic compartments (Shirinpour et al., 2021). We analyzed the number of
302 action potentials, calcium spikes and their peak values. Simulations were run on a high
303 performance computer in the state of Baden-Württemberg, Germany (bwHPC).

304 **Quantification and statistics.** For the analysis of microglia cell density and spine density,
305 cells or spines were counted manually in maximum intensity projections of the confocal image
306 stacks using the 'Cell Counter' plugin of Fiji image processing package [available at
307 https://fiji.sc/; (Schindelin et al., 2012)].

308 Spine head volumes were assessed in the confocal image stacks using the Imaris x64
309 (version 9.5.0) software. The surface tool with the 'split touching object' option enabled was
310 used to measure the volume of spine heads. Files were stored as .ims.

311 Confocal images of PI stained cultures were processed and analyzed using the Fiji
312 image processing package. After background subtraction (rolling ball radius 50 px), images
313 were binarized and PI positive particles were displayed and counted using the 'Analyze
314 Particles' function. Values were normalized to the mean value of the control group.

315 Confocal image stacks of heterozygous *C57BL/6-Tg(TNFa-eGFP)* cultures were
316 processed and analyzed as previously described (Lenz et al., 2020) using the Fiji image
317 processing package. Mean fluorescence intensity of the culture area was normalized to the
318 mean value of fluorescence intensity of the sham-stimulated cultures in the respective round.

319 Dendritic morphologies were assessed using the Neurolucida® 360 software (version
320 2020.1.1). Cells were semi-automatically reconstructed with the 'user guided tree
321 reconstruction' function. Reconstructions were saved as .DAT files and analysis was performed
322 in the Neurolucida Explorer (version 2019.2.1).

323 To analyze microglia morphology in *HexB-tdTom* cultures, confocal image stacks were
324 processed and analyzed using the Fiji image processing package. Of each z-stack a maximum
325 intensity projection was generated and binarized using the 'Trainable Weka Segmentation'
326 plugin (Arganda-Carreras et al., 2017). The same classifier was applied to all images of the
327 same microglia over the recorded 3 h. After removing outliers (radius = 2 px, threshold = 50),
328 microglia scanning density and microglia domain of each image were manually assessed as
329 previously described (Pfeiffer et al., 2016). Values were normalized to the mean.

330 For the analysis of microglial morphology in acute mouse cortical slices, stacks of
331 single cells were also processed and analyzed using the Fiji image processing package. First,
332 each stack was processed using the 'despeckle' function, then a maximum intensity projection
333 was generated. After removing outliers (radius = 3 px, threshold = 50), the image was binarized
334 as described before. Again, outliers were removed (radius = 2 px, threshold = 50), microglia
335 scanning density and microglia domain of each image were manually assessed.

336 Single cell recordings were analyzed off-line using Clampfit 11 of the pClamp11
337 software package (Molecular Devices). sEPSC and mEPSC properties were analyzed using the
338 automated template search tool for event detection (Lenz et al., 2021). Input resistance was
339 calculated for the injection of -100 pA current at a time frame of 200 ms with maximum
340 distance to the Sag-current. Resting membrane potential was calculated as the mean baseline
341 value. AP detection was performed using the input/output curve threshold search event
342 detection tool, and the AP frequency was assessed upon the number of APs detected during the

343 respective injection step. 4 cells in the microglia-depleted (BLZ945-treated) sham stimulated
344 group were excluded in the analysis of intrinsic properties (Figure S4) due to loss of the
345 integrity of the patch during recording of the I-V-curve.

346 Statistical evaluation of the multi-scale modeling was implemented in R (4.0.3;
347 https://www.R-project.org/) and R Studio (1.3.1093; http://www.rstudio.com/) integrated
348 development environment. We ran generalized linear mixed models (GLMM) with predictors
349 TREATMENT (two levels: control, PLX3397) and COMPARTMENT (three levels: soma,
350 apical and basal dendrites). GLMM allows modeling dependent variables from different
351 distributions and model both fixed and random effects (Stroup, 2012). The null model
352 contained the cell as random intercept, and we added each predictor and their interaction terms
353 one-by-one to the subsequent models. The Bayesian information criterion (BIC) was used to
354 compare the current model with the previous one. We selected the winning model if the ΔBIC
355 was at least 10 units less than for the null or previous model.

356 Affymetrix GeneChip™ microarray data (CEL files) were analyzed using the
357 Affymetrix Transcriptome Analysis Console (TAC version 4.0.2.15). Gene expression was
358 considered significantly different when FDR p-value < 0.05 and fold change < -2 or > 2.
359 Differentially expressed well-annotated genes were considered 'microglia-specific' (Figure 1)
360 if they were part of highly specific microglia markers found by Chiu et al. (Chiu et al., 2013)
361 and 'microglia-related' if there was literature found that showed expression of these genes in
362 microglia. A full list of differentially expressed genes including predicted genes is provided in
363 supplementary table 1.

364 RT-qPCR data were analyzed as previously described (Lenz et al., 2020) with the Bio-
365 Rad CFX Maestro 1.0 software package using the ΔΔCq method with *Gapdh* as reference gene.
366 Values were normalized to the mean value of the respective vehicle-treated control group.

367 Mesoscale cytokine detection assay was analyzed using the MSD DISCOVERY
368 WORKBENCH 4.0 platform. mRNA/protein level correlations were visualized by a linear
369 regression fit and analyzed using non-parametric Spearman's correlation coefficients (r).

370 Data were analyzed using GraphPad Prism 7 (GraphPad software, USA). Statistical
371 comparisons were made using non-parametric tests, since normal distribution could not be
372 assured. For column statistics, Mann-Whitney test (to compare two groups) and Kruskal-
373 Wallis-test followed by Dunn's multiple comparisons were used. For statistical comparison of
374 XY-plots, we used an RM two-way ANOVA test (repeated measurements/analysis) with
375 Sidak's multiple comparisons. p-values < 0.05 were considered a significant difference. In the
376 text and figures, values represent mean ± standard error of the mean (s.e.m.). * $p < 0.05$, ** p
377 < 0.01, *** $p < 0.001$ and not significant differences are indicated by 'ns'.

378 **Digital Illustrations.** Figures were prepared using Photoshop graphics software (Adobe, San
379 Jose, CA, USA). Image brightness and contrast were adjusted.

380 **RESULTS**

381 **Pharmacologic depletion of microglia in organotypic tissue cultures**

382 To determine the role of microglia in r(T)MS-induced synaptic plasticity organotypic tissue
383 cultures were treated with the colony-stimulating factor 1 receptor (CSF-1R) antagonist
384 PLX3397, which readily depletes microglia (Coleman et al., 2020; Elmore et al., 2014). Tissue
385 cultures containing the entorhinal cortex and the hippocampus were exposed to 50 nM
386 PLX3397 for at least 18 days *in vitro*, starting immediately after tissue-culture preparation
387 (Figure 1). A robust and almost complete depletion of microglia (~96% reduction in cell
388 density) was observed in the three-week old tissue cultures, as demonstrated by
389 immunostaining for the microglial marker Iba1 (Figure 1B-D).

390 Successful depletion of microglia was also confirmed with RNA microarray analysis
391 (Figure 1E-G). We observed a significant reduction of microglia-specific and microglia-related
392 genes in the group treated with PLX3397 (Figure 1E, F). Specifically, gene sets characteristic
393 of M0-, M1-, and M2-classified microglia (Jurga et al., 2020) were reduced in our tissue
394 cultures (Figure 1G). In turn, no major changes in the expression of genes related to astrocytes,
395 oligodendrocytes, and neurons, i.e., synaptic genes were observed following microglia
396 depletion. These findings show that treatment with PLX3397 results in a robust and specific
397 depletion of microglia in three-week-old organotypic tissue cultures.

398 **CA1 pyramidal neurons in microglia-depleted tissue cultures do not express rMS-**
399 **induced synaptic plasticity**

400 Microglia-depleted tissue cultures and non-depleted control cultures were stimulated with a 10
401 Hz stimulation protocol consisting of 900 pulses at 50% maximum stimulator output using a
402 Magstim Rapid^2 stimulator equipped with an AirFilm® coil (Figure 2). The distance from the

403 coil and the orientation of the stimulated tissue within the electric field were kept constant in
404 all experiments (Figure 2A, B). CA1 pyramidal neurons were patched and α-amino-3-hydroxy-
405 5-methyl-4-isoxazolepropionic acid (AMPA) receptor-mediated miniature excitatory
406 postsynaptic currents (mEPSCs) were recorded 2–4 h after stimulation (Figure 2C). Sham-
407 stimulated controls were treated the same way except for stimulation. In line with previous
408 work (Lenz et al., 2020; Lenz et al., 2015; Vlachos et al., 2012), 10 Hz rMS induced a robust
409 strengthening of excitatory synapses in CA1 pyramidal neurons of control tissue cultures, as
410 demonstrated by increased mean mEPSC amplitude, half width, area, and frequency (Figure
411 3A-C). Conversely, no changes in mEPSCs were observed in microglia-depleted tissue cultures
412 following rMS (Figure 3D-E). These results demonstrate that the presence of microglia is
413 required for rMS-induced synaptic plasticity.

414 **Microglia depletion does not affect cell viability**

415 The neurotrophic and neuroprotective effects of microglia are well recognized in the field (e.g.,
416 (Freria et al., 2020; Jin et al., 2017)). Although no obvious signs of cell death were observed
417 in our experiments and despite the fact that baseline mEPSC properties were comparable
418 between the two groups (c.f., Figure 3C and F), we decided to err on the side of caution and
419 tested for alterations in cell viability as a potential confounding factor of rMS-induced synaptic
420 plasticity. In these experiments propidium iodide (PI) staining was used to assess viability and
421 cell death in our preparations [Figure 4; c.f., (Lenz et al., 2020)]. PI is a cell-membrane
422 impermeant fluorescent molecule that binds to DNA. Hence, PI can be used as a marker for
423 membrane integrity when applied to living tissue. Tissue cultures treated with PLX3397 (50
424 nM) or vehicle-only controls were stained with PI and NMDA treated tissue cultures (50 µM,
425 4 h) served as a positive control in these experiments (Figure 4A). The PI-signal was
426 comparatively low in three-week-old control cultures and age- and time-matched PLX3397-

427 treated preparations, while a significant increase in PI-signal was detected in the NMDA-
428 treated group (Figure 4A). We conclude from these results that the inability of CA1 pyramidal
429 neurons to express rMS-induced synaptic plasticity is not based on altered cell viability or cell
430 death in the absence of microglia.

431 **No major functional and structural changes of CA1 pyramidal neurons in microglia-**
432 **depleted tissue cultures**

433 Neuronal excitability and morphology are expected to have a major impact on the outcome of
434 electromagnetic stimulation (Aberra et al., 2020; Shirinpour et al., 2021). Therefore, we tested
435 for the effect of microglia depletion on structural and functional properties of CA1 pyramidal
436 neurons in our experiments (Figure 4-6). Another set of CA1 pyramidal neurons was recorded
437 in control and microglia-depleted tissue cultures and stained posthoc for morphological
438 analysis (Figure 4B; c.f., Figures 5 and 6).

439 PLX3397-mediated microglia depletion did not affect the basic functional properties of
440 CA1 pyramidal neurons, i.e., resting membrane potential (Figure 4C) and input resistance
441 (Figure 4D). A slight but non-significant difference in action potential frequency was observed
442 for high current injections between the two groups (Figure 4E). Likewise, amplitudes and
443 frequencies of AMPA-receptor mediated spontaneous EPSC were not significantly different
444 between the groups (Figure 4F). These results indicate that microglia depletion does not affect
445 basic functional properties and synaptic activity of CA1 pyramidal neurons.

446 Consistent with these findings, Sholl analysis of the reconstructions of apical and basal
447 dendrites did not show any major effects of microglia depletion on the dendritic morphologies
448 of CA1 pyramidal neurons (Figure 5A, B). We did not observe any significant differences in

449 total dendritic length (Figure 5C), the number of branching points (Figure 5D), or the number
450 of endpoints (Figure 5E).

451 Finally, a detailed morphological analysis of CA1 dendritic spines (Figure 6) confirmed
452 our sEPSC recordings by demonstrating no significant differences in spine densities and spine-
453 head volumes between the two groups in CA1 stratum radiatum (Figure 6A), stratum oriens
454 (Figure 6B) and stratum lacunosum-moleculare (Figure 6C).

455 Taken together, we conclude that microglia depletion does not cause major structural and
456 functional changes in CA1 pyramidal neurons that could readily explain the inability of neurons
457 to express rMS-induced synaptic plasticity in the absence of microglia.

458 **Realistic multi-scale computer modeling predicts no major differences in rMS-induced**
459 **depolarization and intracellular Ca^{2+} levels**

460 We further evaluated the effects of 10 Hz rMS on CA1 pyramidal neurons using multi-scale
461 computational modeling to link the physical input parameters of rMS to dendritic morphologies
462 and subcellular neural effects [Figure 7; (Shirinpour et al., 2021)]. The 3D reconstructed
463 morphologies from recorded CA1 pyramidal neurons in microglia-depleted and non-depleted
464 tissue cultures (c.f., Figure 5) were used in these experiments (Figure 7A). Both membrane
465 voltage and calcium concentrations were assessed in this modeling approach (Figure 7B-F).
466 We estimated the minimum synaptic weight just below the firing threshold of the CA1
467 pyramidal neurons. Consistent with our experimental data the synaptic weights of the model
468 did not differ in CA1 pyramidal neurons from depleted and non-depleted tissue cultures (Figure
469 8D).

470 We compared the peak spike values for the membrane voltage. The winning model
471 ($\Delta BIC = 341.24$; $F_{2,102} = 1387.59$, $p = 2.2 \times 10^{-16}$) employed the compartment as predictor.

472 Confirming our expectations, the analysis revealed significantly weaker peak values in the
473 apical ($t = -48.524$, $p = 2.2 \times 10^{-16}$) and basal dendrites ($t = -6.563$, $p = 2.23 \times 10^{-9}$). However,
474 the treatment had no effect on either the number of spikes (Figure 7D) or the peak action
475 potential values in any compartment (Figure 7E).

476 We continued by comparing the peak calcium-concentration values extracted from the
477 compartments and treatment conditions. As for the voltage data, the winning model ($\Delta BIC =$
478 189.3875; $F_{2,102} = 283.51$, $p = 2.2 \times 10^{-16}$) utilized the compartment as predictor. Again, the
479 analysis revealed significantly weaker peak values in the apical ($t = -21.64$, $p = 2.2 \times 10^{-16}$) and
480 basal dendrites ($t = -19.75$, $p = 2.2 \times 10^{-16}$). However, the treatment had no major effects on
481 the peak calcium-concentration levels in compartments investigated (Figure 7F).

482 **Repetitive magnetic stimulation does not affect structural properties of microglia**

483 After demonstrating that structural and functional differences of CA1 pyramidal neurons do
484 not explain our major findings, i.e., the inability of neurons to express rMS-induced synaptic
485 plasticity in the absence of microglia, we considered the possible effects of rMS on the
486 structural and functional properties of microglia (Figures 8 and 9).

487 To test for the effects of 10 Hz rMS on microglia morphology and dynamics, tissue
488 cultures were prepared from the recently established transgenic *HexB-tdTom* mouse line, which
489 expresses the red fluorescent protein tdTomato under the control of the Hexoaminidase B
490 promotor (HexB) (Masuda et al., 2020). Of all tdTomato expressing cells, 97% also showed a
491 positive Iba1 staining, while in 98% of all Iba1 positive cells, tdTomato signal was also
492 detected (Figure S1). Apparently, the vast majority of microglia are readily identified in three-
493 week-old tissue cultures prepared from *HexB-tdTom* mice.

494 We next employed live-cell microscopy and imaged microglia, i.e., tdTomato
495 expressing cells in CA1 stratum radiatum. Confocal image stacks were obtained every 2
496 minutes for 3 hours immediately after 10 Hz rMS or sham stimulation (Figure 8). In these
497 experiments, we did not observe any major rMS-related changes in microglia morphology. A
498 detailed analysis of microglia dynamics in maximum-intensity projections (Figure 8A-C)
499 revealed no significant changes in dynamic microglial domains and scanning densities among
500 rMS-stimulated and sham-stimulated tissue cultures (Figure 8D). We conclude that 10 Hz rMS
501 does not lead to major changes in microglia morphology and dynamics.

502 **Repetitive magnetic stimulation triggers a release of plasticity-promoting cytokines from**
503 **microglia**

504 We then considered whether 10 Hz rMS triggers an activation of microglia in the absence of
505 major changes in microglia morphology. The plasticity-modulating effects of cytokines
506 secreted by activated microglia are well-established (e.g., Cao et al., 2014; Chai et al., 2019;
507 Habbas et al., 2015; Heir and Stellwagen, 2020; Lenz et al., 2020; Maggio and Vlachos, 2018;
508 Santello et al., 2011; Stellwagen and Malenka, 2006; Tancredi et al., 2000). Specifically, TNFα
509 and IL6 have been linked to the ability of neurons to express synaptic plasticity (Lenz et al.,
510 2015; Rizzo et al., 2018; Stellwagen and Malenka, 2006; Tancredi et al., 2000). In this context,
511 we were recently able to demonstrate that low concentrations of TNFα promote the ability of
512 neurons to express synaptic plasticity (Maggio and Vlachos, 2018). Therefore, we theorized
513 that 10 Hz rMS could trigger the production and/or secretion of TNFα and other cytokines at
514 low, i.e., plasticity-promoting concentrations.

515 We performed qPCR-analyses and protein-detection assays in another set of 10 Hz
516 stimulated and sham-stimulated microglia-depleted and non-depleted tissue cultures (Figure
517 9A-C and Figure S2). Indeed, 10 Hz rMS triggered an increase in TNFα at both the mRNA and

518 protein levels that was not evident in microglia-depleted tissue cultures (Figure 9A). Notably,
519 reduced baseline levels of TNFα protein were observed in the microglia-depleted tissue
520 cultures, which is consistent with the suggestion that microglia are a major source of TNFα in
521 our preparations ($n_{control, non-depleted}$ = 6 cultures, $n_{control, PLX3397}$ = 8 cultures; Mann-Whitney test).
522 Moreover, a considerable increase in IL6 and CXCL1 was detected only in non-depleted tissue
523 cultures (Figure 9B, C). Notably, IL1β could only be detected at the lower detection limit and
524 did not increase significantly upon stimulation.

525 We further excluded an rMS-induced pathological activation of microglia in tissue
526 cultures prepared from a transgenic TNFα reporter mouse line, which expresses the enhanced
527 green fluorescent protein under the control of the TNF-promoter, *C57BL/6-Tg(TNFa-eGFP).*
528 In a previous study, we found a strong pathological activation of microglia, i.e., strong increase
529 in eGFP-expression, in the presence of bacterial lipopolysaccharides (Lenz et al., 2020). Live-
530 cell microscopy revealed no obvious changes in eGFP fluorescence following 10 Hz rMS
531 (Figure 9D), which is in line with a moderate production and release of cytokines (Figure 9A-
532 C) in the absence of obvious morphological changes of microglia (Figure 8). Taken together,
533 these results suggest that 10 Hz rMS induces a physiological increase and release in microglial
534 cytokines, e.g., TNFα and IL6.

535 **Substitution of plasticity-promoting cytokines during stimulation rescues rMS-induced**
536 **synaptic plasticity in microglia-depleted tissue cultures**

537 We then tested whether the exogenous substitution of TNFα and IL6 rescues the ability of CA1
538 pyramidal neurons to express rMS-induced synaptic plasticity in the absence of microglia
539 (Figure 10). TNFα (5 ng/ml) and IL6 (2.5 ng/ml) were added to the medium during stimulation
540 only, and AMPA-receptor mediated mEPSCs were again recorded from CA1 pyramidal
541 neurons of microglia-depleted tissue cultures between 2-4 h after stimulation (Figure 10A).

542 Indeed, in these experiments rMS-induced synaptic strengthening, i.e., a significant increase in
543 mean mEPSC amplitude and half width was observed (Figure 10B). Of note, exposure to TNFα
544 and IL6 at the same concentration and duration did not affect mEPSC amplitudes; only mEPSC
545 frequencies were increased (n_{sham} = 20 cells, $n_{sham+cytokines}$ = 22 cells; mEPSC amplitude: 24.27
546 ± 0.56 pA (sham) vs. 24.86 ± 0.43 pA (sham+cytokines), ns; mEPSC frequency: 0.81 ± 0.06
547 Hz (sham) vs. 0.95 ± 0.05 Hz (sham+cytokines), $p < 0.05$*; Mann-Whitney test). We conclude
548 that TNFα and IL6 released from microglia during stimulation is required for rMS-induced
549 synaptic potentiation.

550 ***In vivo* microglia depletion prevents rTMS-induced excitatory synaptic plasticity in the**
551 **mouse mPFC**

552 Finally, we tested whether the presence of microglia is required for rTMS-induced plasticity of
553 synaptic transmission *in vivo* (Figure 12; Kloosterboer and Funke, 2019; Lenz et al., 2016;
554 Thimm and Funke, 2015). *In vivo* microglia depletion was achieved through daily application
555 of the CSF-1R inhibitor BLZ945 (200 mg kg^{-1}, oral gavage, for 7 consecutive days prior to
556 experimental assessment; Hagemeyer et al., 2017; Masuda et al., 2020). Anesthetized
557 microglia-depleted and non-depleted mice were stimulated with the same 10 Hz stimulation
558 protocol as in our *in vitro* experiments. Two hours after the stimulation, frontal brain sections
559 containing the medial prefrontal cortex were prepared and AMPA-receptor meditated sEPSCs
560 were recorded from superficial pyramidal neurons of the mPFC (3-5 hours post stimulation;
561 Figure 11A). BLZ945-induced microglia depletion was confirmed by Iba1 stainings of frontal
562 brain sections (~90% reduction in cell density in the BLZ945-treated animals; Figure 11B).
563 While *in vivo* microglia-depletion had no significant effects on baseline synaptic transmission,
564 a significant increase in sEPSC frequencies was not observed in the stimulated microglia-
565 depleted animals. Notably, the mean sEPSC amplitude remained unaltered in microglia-

566 depleted and non-depleted animals (Figure 11C). Amplitude-frequency plots confirmed that
567 rTMS promoted an amplitude-independent increase in sEPSC frequencies which was absent -
568 if not reversed - in the mPFC of microglia-depleted animals (Figure 11C, D). These changes
569 occurred in the absence of major changes in active and passive membrane properties in
570 microglia-depleted and non-depleted animals (Figure S3). Similar to our *in vitro* experiments
571 in hippocampal area CA1, no rTMS-induced changes in microglia morphologies were observed
572 in the mPFC of anesthetized mice (Figure S4). These results demonstrate the essential, i.e.,
573 plasticity-promoting, role of microglia for rTMS-induced changes in network activity and
574 neurotransmission.

575 **DISCUSSION**

576 The experiments of this study demonstrate that the presence of microglia is required for the
577 induction of synaptic plasticity triggered by 10 Hz rTMS in brain tissue of mice (*in vitro* and
578 *in vivo*). In this context, a robust functional activation of microglia was observed as reflected
579 by the gene expression and release of TNFα and IL6 (but not IL1b). Indeed, substitution of
580 TNFα and IL6 rescued the ability of neurons to express synaptic plasticity in microglia-
581 depleted brain tissue cultures. The changes occurred in the absence of major morphological
582 and functional changes of the stimulated neurons in the microglia-depleted brain tissue, and no
583 obvious changes of microglia morphologies and their dynamics were observed after 10 Hz
584 electromagnetic stimulation. These results demonstrate that rTMS effectively modulates
585 microglia function, i.e., cytokine release, in stimulated brain regions, thereby identifying a
586 novel mechanism of action which may explain some of the beneficial effects of rTMS seen in
587 healthy individuals and in patients.

588 During recent years experimental evidence has suggested that rTMS-induced after-
589 effects are mediated by "LTP-like" plasticity mechanisms (Ziemann, 2004). This evidence is
590 based on physiological characteristics and pharmacological analogies between studies
591 performed at the system level in human subjects (Brown et al., 2020; Korchounov and
592 Ziemann, 2011; Ziemann et al., 2015) and data obtained from animal models (Hoogendam et
593 al., 2010; Vlachos et al., 2012). Specifically, the effects of pharmacological modulation of
594 NMDA receptors have been interpreted as evidence for "LTP-like" plasticity, considering the
595 relevance of NMDA receptors in LTP-induction (Brown et al., 2020; Lenz et al., 2015; Vlachos
596 et al., 2012). Our own past work demonstrated that pharmacological inhibition of NMDA
597 receptors or L-Type voltage-gated calcium channels block the ability of neurons to express
598 synaptic plasticity induced by 10 Hz rMS (Lenz et al., 2015; Vlachos et al., 2012). Consistent

599 with these findings, stimulation in Ca^{2+}-free external solution failed to induce synaptic
600 plasticity, thus confirming the relevance of Ca^{2+}-dependent signaling pathways in rMS-induced
601 synaptic plasticity (Lenz et al., 2015). Notably, NMDA receptors and L-Type voltage-gated
602 calcium channels are also expressed on microglia (Hopp, 2021; Murugan et al., 2011). In fact,
603 robust experimental evidence exists demonstrating that the modulation of intracellular Ca^{2+}
604 levels regulate important microglia functions (Laprell et al., 2021). Hence, some of the results
605 obtained in animal models and human studies could be explained—at least in part—by
606 differential regulation of calcium signaling in microglia and neurons. In this context, additional
607 research is required to clarify whether rTMS acts on microglia directly or whether microglia
608 are activated indirectly by sensing rTMS-induced changes in neuronal activity, e.g., via
609 microglial glutamate receptors, purinergic receptors, or other signaling pathways (Cserep et al.,
610 2020).

611 Regardless of these considerations, the present study demonstrates that the presence of
612 microglia is required for rTMS-induced synaptic plasticity: CA1 pyramidal neurons in
613 microglia-depleted tissue cultures as well as superficial pyramidal neurons in the mPFC of
614 adult mice did not express rTMS-induced excitatory synaptic plasticity. These findings support
615 the recently emphasized impact of glial cells on the neural effects of non-invasive brain
616 stimulation (Gellner et al., 2021). Interestingly, we did not observe any obvious signs of
617 functional and structural alterations of CA1 pyramidal neurons in microglia-depleted tissue
618 cultures. Consistent with these findings, multi-scale compartmental modeling confirmed that
619 basic morphological and functional properties of neurons do not explain the inability of CA1
620 pyramidal neurons to express rMS-induced plasticity. We must concede, however, that detailed
621 morphological reconstructions of axons were not obtained, as it is difficult to reliably visualize
622 and reconstruct the entire axon morphology of individual neurons. Indeed, computational
623 studies emphasize the relevance of axons and myelination in rTMS-induced synaptic plasticity

624 (Aberra et al., 2020; Fields, 2005; Shirinpour et al., 2021; Wang et al., 2018). It should be
625 noted, though, that we did not observe any differences in network activity in our experimental
626 setting, as neither sEPSC amplitudes nor frequencies were affected in microglia-depleted tissue
627 cultures. Consistent with these findings we did not observe any differences in dendritic spine
628 counts, and no evidence for alterations in oligodendrocyte markers was obtained in our RNA
629 microarray analysis of microglia-depleted tissue cultures. It is thus unlikely that major changes
630 in the structural and functional properties of CA1 pyramidal neurons explain our results,
631 especially considering our rescue experiments in which only short exposure to TNFα and IL6
632 during stimulation was sufficient to restore rMS-induced synaptic plasticity in the absence of
633 microglia.

634 10 Hz rMS induced a robust increase in immune-mediator gene expression and TNFα
635 and IL6 release in organotypic tissue cultures, suggesting that rMS activates microglia.
636 Previous studies have demonstrated that proinflammatory cytokines influence excitatory
637 neurotransmission (Cao et al., 2014; Maggio and Vlachos, 2018; Riazi et al., 2015; Sheppard
638 et al., 2019; Stellwagen and Malenka, 2006; Strehl et al., 2014). Specifically, TNFα and IL6
639 have been implicated as important secreted factors that modulate synaptic transmission
640 (Furukawa and Mattson, 1998; Garcia-Oscos et al., 2012; Stellwagen et al., 2005) and plasticity
641 (Heir and Stellwagen, 2020). In this context it has been shown that TNFα acts as a permissive
642 factor (Becker et al., 2013; Steinmetz and Turrigiano, 2010), where TNFα *per se* does not
643 trigger major changes in postsynaptic strength; rather, it modulates the ability of neurons to
644 express plasticity without affecting baseline synaptic transmission; besides changes in
645 presynaptic glutamate release (Santello et al., 2011) as also reflected by the increased mEPSC
646 frequencies seen in our experiments, in which microglia-depleted tissue cultures were exposed
647 to TNFα and IL6 without stimulation. Indeed, experiments employing classic tetanic electric
648 stimulation showed that low concentrations of TNFα rapidly promote LTP-induction, while

649 high concentrations of TNFα impede the ability of neurons to express LTP (Maggio and
650 Vlachos, 2018). These findings are consistent with the metaplastic effects of TNFα. In line with
651 this suggestion, pathological activation of microglia with bacterial lipopolysaccharides, which
652 triggers strong TNFα production, i.e., ~10–15 fold increase in TNFα-mRNA and ~2000 fold
653 increase in TNFα protein levels, occludes the ability of CA1 pyramidal neurons to express 10
654 Hz rMS-induced synaptic plasticity (Lenz et al., 2020). Together with the results of the present
655 study, these findings demonstrate that microglia have an important role in rTMS-induced
656 synaptic plasticity. They call for a systematic assessment of rTMS-induced microglia plasticity,
657 and raise the intriguing possibility that rTMS recruits metaplasticity by activating microglia
658 (directly or indirectly). Hence, some of the beneficial effects of rTMS seen in patients may
659 reside—at least in part—in the effects of rTMS on microglia function, which also seem to be
660 involved in promoting the ability of neurons to express "LTP-like" plasticity shortly after
661 stimulation.

662 **DECLARATIONS**

663 **Acknowledgements:** We thank Simone Zenker for skillful technical assistance and the Next
664 Generation Sequencing Core Facility (NGS-CF, Faculty of Medicine, University of Freiburg)
665 for assistance in transcriptome analysis. The authors also acknowledge the support by the state
666 of Baden-Württemberg through the possibility of using high performance computing resources
667 (bwHPC; bwUniCluster 2.0).

668 **Funding:** This work was supported by MOTI-VATE graduate school, Faculty of Medicine,
669 University of Freiburg (to AE), the EQUIP Medical Scientist Programme, Faculty of Medicine,
670 University of Freiburg (to ML), Faculty of Medicine of the University of Freiburg
671 (TUR217/21; to ZT), and Deutsche Forschungsgemeinschaft (DFG; Project-ID 259373024
672 B14–CRC/TRR 167; to AV).

673 **Author Contributions:** Author contributions have been assigned according to CRediT
674 taxonomy. AE: Validation, Formal Analysis, Investigation, Writing-original draft preparation,
675 Visualization, Funding acquisition. DK: Investigation. ZT: Investigation, Formal Analysis.
676 MF: Investigation. MK: Investigation, Formal Analysis. DP: Resources. TM: Resources. MP:
677 Resources. ML: Conceptualization, Methodology, Validation, Formal Analysis, Investigation,
678 Writing-original draft preparation, Visualization, Supervision, Project administration, Funding
679 acquisition. AV: Conceptualization, Methodology, Resources, Writing-original draft
680 preparation, Supervision, Project administration, Funding acquisition.

681 **Declarations of interest:** none.

682 **REFERENCES**

683 Aberra, A.S., Wang, B., Grill, W.M., and Peterchev, A.V. (2020). Simulation of transcranial magnetic
684 stimulation in head model with morphologically-realistic cortical neurons. Brain Stimul *13*, 175-189.

685 Akiyoshi, R., Wake, H., Kato, D., Horiuchi, H., Ono, R., Ikegami, A., Haruwaka, K., Omori, T.,
686 Tachibana, Y., Moorhouse, A.J.*, et al.* (2018). Microglia Enhance Synapse Activity to Promote Local
687 Network Synchronization. eNeuro *5*.

688 Arganda-Carreras, I., Kaynig, V., Rueden, C., Eliceiri, K.W., Schindelin, J., Cardona, A., and Sebastian
689 Seung, H. (2017). Trainable Weka Segmentation: a machine learning tool for microscopy pixel
690 classification. Bioinformatics *33*, 2424-2426.

691 Badimon, A., Strasburger, H.J., Ayata, P., Chen, X., Nair, A., Ikegami, A., Hwang, P., Chan, A.T.,
692 Graves, S.M., Uweru, J.O.*, et al.* (2020). Negative feedback control of neuronal activity by microglia.
693 Nature *586*, 417-423.

694 Becker, D., Zahn, N., Deller, T., and Vlachos, A. (2013). Tumor necrosis factor alpha maintains
695 denervation-induced homeostatic synaptic plasticity of mouse dentate granule cells. Front Cell Neurosci
696 *7*, 257.

697 Brown, J.C., DeVries, W.H., Korte, J.E., Sahlem, G.L., Bonilha, L., Short, E.B., and George, M.S.
698 (2020). NMDA receptor partial agonist, d-cycloserine, enhances 10 Hz rTMS-induced motor plasticity,
699 suggesting long-term potentiation (LTP) as underlying mechanism. Brain Stimul *13*, 530-532.

700 Cao, D.L., Zhang, Z.J., Xie, R.G., Jiang, B.C., Ji, R.R., and Gao, Y.J. (2014). Chemokine CXCL1
701 enhances inflammatory pain and increases NMDA receptor activity and COX-2 expression in spinal
702 cord neurons via activation of CXCR2. Exp Neurol *261*, 328-336.

703 Chai, H.H., Fu, X.C., Ma, L., Sun, H.T., Chen, G.Z., Song, M.Y., Chen, W.X., Chen, Y.S., Tan, M.X.,
704 Guo, Y.W.*, et al.* (2019). The chemokine CXCL1 and its receptor CXCR2 contribute to chronic stress-
705 induced depression in mice. FASEB J *33*, 8853-8864.

706 Chiu, I.M., Morimoto, E.T., Goodarzi, H., Liao, J.T., O'Keeffe, S., Phatnani, H.P., Muratet, M., Carroll,
707 M.C., Levy, S., Tavazoie, S.*, et al.* (2013). A neurodegeneration-specific gene-expression signature of
708 acutely isolated microglia from an amyotrophic lateral sclerosis mouse model. Cell Rep *4*, 385-401.

709 Cirillo, G., Di Pino, G., Capone, F., Ranieri, F., Florio, L., Todisco, V., Tedeschi, G., Funke, K., and
710 Di Lazzaro, V. (2017). Neurobiological after-effects of non-invasive brain stimulation. Brain Stimul
711 *10*, 1-18.

712 Clarke, D., Penrose, M.A., Harvey, A.R., Rodger, J., and Bates, K.A. (2017). Low intensity rTMS has
713 sex-dependent effects on the local response of glia following a penetrating cortical stab injury. Exp
714 Neurol *295*, 233-242.

715 Coleman, L.G., Jr., Zou, J., and Crews, F.T. (2020). Microglial depletion and repopulation in brain slice
716 culture normalizes sensitized proinflammatory signaling. J Neuroinflammation *17*, 27.

717 Cserep, C., Posfai, B., Lenart, N., Fekete, R., Laszlo, Z.I., Lele, Z., Orsolits, B., Molnar, G., Heindl, S.,
718 Schwarcz, A.D.*, et al.* (2020). Microglia monitor and protect neuronal function through specialized
719 somatic purinergic junctions. Science *367*, 528-537.

720 Cullen, C.L., and Young, K.M. (2016). How Does Transcranial Magnetic Stimulation Influence Glial
721 Cells in the Central Nervous System? Front Neural Circuits *10*, 26.

722 Elmore, M.R., Najafi, A.R., Koike, M.A., Dagher, N.N., Spangenberg, E.E., Rice, R.A., Kitazawa, M.,
723 Matusow, B., Nguyen, H., West, B.L.*, et al.* (2014). Colony-stimulating factor 1 receptor signaling is
724 necessary for microglia viability, unmasking a microglia progenitor cell in the adult brain. Neuron *82*,
725 380-397.

726 Fields, R.D. (2005). Myelination: an overlooked mechanism of synaptic plasticity? Neuroscientist *11*,
727 528-531.

728 Forster, E., Zhao, S., and Frotscher, M. (2006). Laminating the hippocampus. Nat Rev Neurosci *7*, 259-
729 267.

730 Freria, C.M., Brennan, F.H., Sweet, D.R., Guan, Z., Hall, J.C., Kigerl, K.A., Nemeth, D.P., Liu, X.,
731 Lacroix, S., Quan, N.*, et al.* (2020). Serial Systemic Injections of Endotoxin (LPS) Elicit
732 Neuroprotective Spinal Cord Microglia through IL-1-Dependent Cross Talk with Endothelial Cells. J
733 Neurosci *40*, 9103-9120.

734 Furukawa, K., and Mattson, M.P. (1998). The transcription factor NF-kappaB mediates increases in
735 calcium currents and decreases in NMDA- and AMPA/kainate-induced currents induced by tumor
736 necrosis factor-alpha in hippocampal neurons. J Neurochem *70*, 1876-1886.

737 Garcia-Oscos, F., Salgado, H., Hall, S., Thomas, F., Farmer, G.E., Bermeo, J., Galindo, L.C., Ramirez,
738 R.D., D'Mello, S., Rose-John, S.*, et al.* (2012). The stress-induced cytokine interleukin-6 decreases the
739 inhibition/excitation ratio in the rat temporal cortex via trans-signaling. Biol Psychiatry *71*, 574-582.

740 Gellner, A.K., Reis, J., Fiebich, B.L., and Fritsch, B. (2021). Electrified microglia: Impact of direct
741 current stimulation on diverse properties of the most versatile brain cell. Brain Stimul *14*, 1248-1258.

742 Graeber, M.B., and Streit, W.J. (2010). Microglia: biology and pathology. Acta Neuropathol *119*, 89-
743 105.

744 Habbas, S., Santello, M., Becker, D., Stubbe, H., Zappia, G., Liaudet, N., Klaus, F.R., Kollias, G.,
745 Fontana, A., Pryce, C.R., *et al.* (2015). Neuroinflammatory TNFalpha Impairs Memory via Astrocyte
746 Signaling. Cell *163*, 1730-1741.

747 Hagemeyer, N., Hanft, K.M., Akriditou, M.A., Unger, N., Park, E.S., Stanley, E.R., Staszewski, O.,
748 Dimou, L., and Prinz, M. (2017). Microglia contribute to normal myelinogenesis and to oligodendrocyte
749 progenitor maintenance during adulthood. Acta Neuropathol *134*, 441-458.

750 Heir, R., and Stellwagen, D. (2020). TNF-Mediated Homeostatic Synaptic Plasticity: From in vitro to
751 in vivo Models. Front Cell Neurosci *14*, 565841.

752 Hildebrandt-Einfeldt, L., Yap, K., Paul, M.H., Stoffer, C., Zahn, N., Drakew, A., Lenz, M., Vlachos,
753 A., and Deller, T. (2021). Crossed Entorhino-Dentate Projections Form and Terminate With Correct
754 Layer-Specificity in Organotypic Slice Cultures of the Mouse Hippocampus. Front Neuroanat *15*,
755 637036.

756 Hoogendam, J.M., Ramakers, G.M., and Di Lazzaro, V. (2010). Physiology of repetitive transcranial
757 magnetic stimulation of the human brain. Brain Stimul *3*, 95-118.

758 Hopp, S.C. (2021). Targeting microglia L-type voltage-dependent calcium channels for the treatment
759 of central nervous system disorders. J Neurosci Res *99*, 141-162.

760 Jin, W.N., Shi, S.X., Li, Z., Li, M., Wood, K., Gonzales, R.J., and Liu, Q. (2017). Depletion of microglia
761 exacerbates postischemic inflammation and brain injury. J Cereb Blood Flow Metab *37*, 2224-2236.

762 Jurga, A.M., Paleczna, M., and Kuter, K.Z. (2020). Overview of General and Discriminating Markers
763 of Differential Microglia Phenotypes. Front Cell Neurosci *14*, 198.

764 Kloosterboer, E., and Funke, K. (2019). Repetitive transcranial magnetic stimulation recovers cortical
765 map plasticity induced by sensory deprivation due to deafferentiation. J Physiol *597*, 4025-4051.

766 Korchounov, A., and Ziemann, U. (2011). Neuromodulatory neurotransmitters influence LTP-like
767 plasticity in human cortex: a pharmaco-TMS study. Neuropsychopharmacology *36*, 1894-1902.

768 Laprell, L., Schulze, C., Brehme, M.L., and Oertner, T.G. (2021). The role of microglia membrane
769 potential in chemotaxis. J Neuroinflammation *18*, 21.

770 Lenz, M., Eichler, A., Kruse, P., Strehl, A., Rodriguez-Rozada, S., Goren, I., Yogev, N., Frank, S.,
771 Waisman, A., Deller, T., *et al.* (2020). Interleukin 10 Restores Lipopolysaccharide-Induced Alterations
772 in Synaptic Plasticity Probed by Repetitive Magnetic Stimulation. Front Immunol *11*, 614509.

773 Lenz, M., Galanis, C., Muller-Dahlhaus, F., Opitz, A., Wierenga, C.J., Szabo, G., Ziemann, U., Deller,
774 T., Funke, K., and Vlachos, A. (2016). Repetitive magnetic stimulation induces plasticity of inhibitory
775 synapses. Nat Commun *7*, 10020.

776 Lenz, M., Kruse, P., Eichler, A., Straehle, J., Beck, J., Deller, T., and Vlachos, A. (2021). All-trans
777 retinoic acid induces synaptic plasticity in human cortical neurons. Elife *10*.

778 Lenz, M., Platschek, S., Priesemann, V., Becker, D., Willems, L.M., Ziemann, U., Deller, T., Muller-
779 Dahlhaus, F., Jedlicka, P., and Vlachos, A. (2015). Repetitive magnetic stimulation induces plasticity
780 of excitatory postsynapses on proximal dendrites of cultured mouse CA1 pyramidal neurons. Brain
781 Struct Funct *220*, 3323-3337.

782 Li, K., Wang, X., Jiang, Y., Zhang, X., Liu, Z., Yin, T., and Yang, Z. (2021). Early intervention
783 attenuates synaptic plasticity impairment and neuroinflammation in 5xFAD mice. J Psychiatr Res *136*,
784 204-216.

785 Maggio, N., and Vlachos, A. (2018). Tumor necrosis factor (TNF) modulates synaptic plasticity in a
786 concentration-dependent manner through intracellular calcium stores. J Mol Med (Berl) *96*, 1039-1047.

787 Masuda, T., Amann, L., Sankowski, R., Staszewski, O., Lenz, M., P, D.E., Snaidero, N., Costa Jordao,
788 M.J., Bottcher, C., Kierdorf, K.*, et al.* (2020). Novel Hexb-based tools for studying microglia in the
789 CNS. Nat Immunol *21*, 802-815.

790 Maus, L., Lee, C., Altas, B., Sertel, S.M., Weyand, K., Rizzoli, S.O., Rhee, J., Brose, N., Imig, C., and
791 Cooper, B.H. (2020). Ultrastructural Correlates of Presynaptic Functional Heterogeneity in
792 Hippocampal Synapses. Cell Rep *30*, 3632-3643 e3638.

793 Muller-Dahlhaus, F., and Vlachos, A. (2013). Unraveling the cellular and molecular mechanisms of
794 repetitive magnetic stimulation. Front Mol Neurosci *6*, 50.

795 Muri, L., Oberhansli, S., Buri, M., Le, N.D., Grandgirard, D., Bruggmann, R., Muri, R.M., and Leib,
796 S.L. (2020). Repetitive transcranial magnetic stimulation activates glial cells and inhibits neurogenesis
797 after pneumococcal meningitis. PLoS One *15*, e0232863.

798 Murugan, M., Sivakumar, V., Lu, J., Ling, E.A., and Kaur, C. (2011). Expression of N-methyl D-
799 aspartate receptor subunits in amoeboid microglia mediates production of nitric oxide via NF-kappaB
800 signaling pathway and oligodendrocyte cell death in hypoxic postnatal rats. Glia *59*, 521-539.

801 Pell, G.S., Roth, Y., and Zangen, A. (2011). Modulation of cortical excitability induced by repetitive
802 transcranial magnetic stimulation: influence of timing and geometrical parameters and underlying
803 mechanisms. Prog Neurobiol *93*, 59-98.

804 Pfeiffer, T., Avignone, E., and Nagerl, U.V. (2016). Induction of hippocampal long-term potentiation
805 increases the morphological dynamics of microglial processes and prolongs their contacts with dendritic
806 spines. Sci Rep *6*, 32422.

807 Prinz, M., Jung, S., and Priller, J. (2019). Microglia Biology: One Century of Evolving Concepts. Cell
808 *179*, 292-311.

809 Prinz, M., Masuda, T., Wheeler, M.A., and Quintana, F.J. (2021). Microglia and Central Nervous
810 System-Associated Macrophages-From Origin to Disease Modulation. Annu Rev Immunol *39*, 251-
811 277.

812 Riazi, K., Galic, M.A., Kentner, A.C., Reid, A.Y., Sharkey, K.A., and Pittman, Q.J. (2015). Microglia-
813 dependent alteration of glutamatergic synaptic transmission and plasticity in the hippocampus during
814 peripheral inflammation. J Neurosci *35*, 4942-4952.

815 Rizzo, F.R., Musella, A., De Vito, F., Fresegna, D., Bullitta, S., Vanni, V., Guadalupi, L., Stampanoni
816 Bassi, M., Buttari, F., Mandolesi, G.*, et al.* (2018). Tumor Necrosis Factor and Interleukin-1beta
817 Modulate Synaptic Plasticity during Neuroinflammation. Neural Plast *2018*, 8430123.

818 Santello, M., Bezzi, P., and Volterra, A. (2011). TNFalpha controls glutamatergic gliotransmission in
819 the hippocampal dentate gyrus. Neuron *69*, 988-1001.

820 Schafer, D.P., Lehrman, E.K., Kautzman, A.G., Koyama, R., Mardinly, A.R., Yamasaki, R., Ransohoff,
821 R.M., Greenberg, M.E., Barres, B.A., and Stevens, B. (2012). Microglia sculpt postnatal neural circuits
822 in an activity and complement-dependent manner. Neuron *74*, 691-705.

823 Schindelin, J., Arganda-Carreras, I., Frise, E., Kaynig, V., Longair, M., Pietzsch, T., Preibisch, S.,
824 Rueden, C., Saalfeld, S., Schmid, B.*, et al.* (2012). Fiji: an open-source platform for biological-image
825 analysis. Nat Methods *9*, 676-682.

826 Sheppard, O., Coleman, M.P., and Durrant, C.S. (2019). Lipopolysaccharide-induced
827 neuroinflammation induces presynaptic disruption through a direct action on brain tissue involving
828 microglia-derived interleukin 1 beta. J Neuroinflammation *16*, 106.

829 Shirinpour, S., Hananeia, N., Rosado, J., Tran, H., Galanis, C., Vlachos, A., Jedlicka, P., Queisser, G.,
830 and Opitz, A. (2021). Multi-scale modeling toolbox for single neuron and subcellular activity under
831 Transcranial Magnetic Stimulation. Brain Stimul.

832 Steinmetz, C.C., and Turrigiano, G.G. (2010). Tumor necrosis factor-alpha signaling maintains the
833 ability of cortical synapses to express synaptic scaling. J Neurosci *30*, 14685-14690.

834 Stellwagen, D., Beattie, E.C., Seo, J.Y., and Malenka, R.C. (2005). Differential regulation of AMPA
835 receptor and GABA receptor trafficking by tumor necrosis factor-alpha. J Neurosci *25*, 3219-3228.

836 Stellwagen, D., and Malenka, R.C. (2006). Synaptic scaling mediated by glial TNF-alpha. Nature *440*,
837 1054-1059.

838 Stevanovic, I., Mancic, B., Ilic, T., Milosavljevic, P., Lavrnja, I., Stojanovic, I., and Ninkovic, M.
839 (2019). Theta burst stimulation influence the expression of BDNF in the spinal cord on the experimental
840 autoimmune encephalomyelitis. Folia Neuropathol *57*, 129-145.

841 Stowell, R.D., Sipe, G.O., Dawes, R.P., Batchelor, H.N., Lordy, K.A., Whitelaw, B.S., Stoessel, M.B.,
842 Bidlack, J.M., Brown, E., Sur, M.*, et al.* (2019). Noradrenergic signaling in the wakeful state inhibits
843 microglial surveillance and synaptic plasticity in the mouse visual cortex. Nat Neurosci *22*, 1782-1792.

844 Strehl, A., Lenz, M., Itsekson-Hayosh, Z., Becker, D., Chapman, J., Deller, T., Maggio, N., and
845 Vlachos, A. (2014). Systemic inflammation is associated with a reduction in Synaptopodin expression
846 in the mouse hippocampus. Exp Neurol *261*, 230-235.

847 Stroup, W.W. (2012). Generalized Linear Mixed Models: Modern Concepts, Methods and
848 Applications. CRC Press.

849 Tancredi, V., D'Antuono, M., Cafe, C., Giovedi, S., Bue, M.C., D'Arcangelo, G., Onofri, F., and
850 Benfenati, F. (2000). The inhibitory effects of interleukin-6 on synaptic plasticity in the rat hippocampus
851 are associated with an inhibition of mitogen-activated protein kinase ERK. J Neurochem *75*, 634-643.

852 Thimm, A., and Funke, K. (2015). Multiple blocks of intermittent and continuous theta-burst
853 stimulation applied via transcranial magnetic stimulation differently affect sensory responses in rat
854 barrel cortex. J Physiol *593*, 967-985.

855 Ting, J.T., Lee, B.R., Chong, P., Soler-Llavina, G., Cobbs, C., Koch, C., Zeng, H., and Lein, E. (2018).
856 Preparation of Acute Brain Slices Using an Optimized N-Methyl-D-glucamine Protective Recovery
857 Method. J Vis Exp.

858 Vlachos, A., Muller-Dahlhaus, F., Rosskopp, J., Lenz, M., Ziemann, U., and Deller, T. (2012).
859 Repetitive magnetic stimulation induces functional and structural plasticity of excitatory postsynapses
860 in mouse organotypic hippocampal slice cultures. J Neurosci *32*, 17514-17523.

861 Wang, B., Grill, W.M., and Peterchev, A.V. (2018). Coupling Magnetically Induced Electric Fields to
862 Neurons: Longitudinal and Transverse Activation. Biophys J *115*, 95-107.

863 Ziemann, U. (2004). TMS induced plasticity in human cortex. Rev Neurosci *15*, 253-266.

864 Ziemann, U., Reis, J., Schwenkreis, P., Rosanova, M., Strafella, A., Badawy, R., and Muller-Dahlhaus,
865 F. (2015). TMS and drugs revisited 2014. Clin Neurophysiol *126*, 1847-1868.

866

867

868

869 **FIGURE LEGENDS**

870 **Figure 1: PLX3397 depletes microglia in organotypic tissue cultures**

871 (A) Entorhino-hippocampal tissue culture stained with DAPI nuclear stain (EC, entorhinal
872 cortex; DG, dentate gyrus). Scale bar, 200 µm.

873 (B, C) Representative examples of tissue cultures stained for the microglial marker Iba1. Note
874 homogenous distribution of microglia in the control culture and almost complete depletion of
875 microglia following PLX3397 treatment (50 nM, 18 days). Scale bars, 200 µm.

876 (D) Microglia cell counts in the respective groups ($n_{control}$ = 14 cultures, $n_{PLX(50nM)}$ = 15 cultures;
877 Mann-Whitney test, U = 0).

878 (E-G) Affymetrix® Microarray analysis of control cultures and cultures treated with PLX3397.
879 (E) Volcano plot shows fold changes and FDR p-values of analyzed transcripts. Significantly
880 upregulated transcripts are indicated in green, significantly downregulated transcripts are
881 indicated in red. (F) Classification of differentially expressed transcripts. 97.5% of the
882 differentially expressed transcripts are microglia-specific or microglia-related. (G) Hierarchical
883 clustering of differentially expressed gene sets characteristic of M0-, M1-, and M2-classified
884 microglia. Each sample consisted of 3 pooled cultures (n = 3 samples in each group).

885 Individual data points are indicated by colored dots. Values represent mean ± s.e.m (***$p <$
886 0.001).

887 **Figure 2: 10 Hz repetitive magnetic stimulation in organotypic tissue cultures**

888 (A-B) Entorhino-hippocampal tissue cultures (DAPI nuclear stain, B) were stimulated with a
889 70 mm outer wing diameter figure of eight coil (Magstim Company, UK). Filter inserts carrying
890 2–6 tissue cultures were placed in a Petri Dish below the coil. The orientation within the
891 electromagnetic field and distance to the coil was kept constant in all experiments (DAPI
892 nuclear stain). Scale bar, 200 µm.

893 (C) Sham stimulated cultures were not stimulated but otherwise treated equally. After
894 stimulation, cultures were kept in the incubator for 2-4 h before further experimental
895 procedures like patch-clamp recordings.

896 **Figure 3: CA1 pyramidal neurons in microglia-depleted tissue cultures do not express**
897 **excitatory synaptic plasticity induced by 10 Hz repetitive magnetic stimulation (rMS)**

898 (A) Example of a recorded and posthoc stained CA1 pyramidal neuron in a tissue culture
899 stained with the microglial marker Iba1. Scale bar, 100 µm.

900 (B, C) Sample traces and group data of AMPA receptor-mediated miniature excitatory
901 postsynaptic currents (mEPSCs) recorded from CA1 pyramidal neurons in sham-stimulated
902 and 10 Hz rMS-stimulated cultures 2-4 h after stimulation ($n_{control\text{-}sham}$ = 56 cells, $n_{control\text{-}rMS}$ =
903 60 cells; Mann-Whitney test, $U_{amplitude}$ = 1091, $U_{half\ width}$ = 1042, U_{area} = 956, $U_{frequency}$ = 651;
904 RM two-way ANOVA followed by Sidak's multiple comparisons test for amplitude-
905 frequency-plot).

906 (D) Example of a recorded and posthoc stained CA1 pyramidal neuron in a PLX3397 treated,
907 microglia-depleted tissue culture stained with the microglial marker Iba1. Scale bar, 100 µm.

908 (E, F) Representative traces and group data of AMPA receptor-mediated mEPSCs recorded
909 from CA1 pyramidal cells in sham-stimulated and 10 Hz rMS-stimulated microglia-depleted
910 tissue cultures 2-4 h after stimulation ($n_{PLX3397\text{-}sham}$ = 61 cells, $n_{PLX3397\text{-}rMS}$ = 55 cells; Mann-
911 Whitney test; RM two-way ANOVA followed by Sidak's multiple comparisons test for
912 amplitude-frequency-plot).

913 Individual data points are indicated by grey dots. Values represent mean ± s.e.m (** $p < 0.01$,
914 *** $p < 0.001$; ns, not significant differences).

915 **Figure 4: Depletion of microglia does not affect cell viability and basic functional**
916 **properties of CA1 pyramidal neurons**

917 (A) Tissue cultures stained with propidium iodide [left: vehicle control, middle: PLX3397 (50
918 nM, 18 d), right: NMDA (50 µM, 4 h)], group data of the quantified propidium iodide signals
919 is shown in the graph on the right ($n_{control}$ = 29 cultures, $n_{PLX(50nM)}$ = 28 cultures, n_{NMDA} = 16
920 cultures; Kruskal-Wallis-test followed by Dunn's post-hoc correction). Scale bars, 200 µm.

921 (B) Examples of patched, recorded and posthoc identified CA1 pyramidal neurons. Scale bar,
922 100 µm.

923 (C, D) Group data of passive membrane properties of CA1 pyramidal neurons in microglia-
924 depleted, i.e., PLX3397 (50 nM, 18 days) treated tissue cultures and control cultures ($n_{control}$ =
925 33 cells, $n_{PLX3397}$= 30 cells; Mann-Whitney test).

926 (E) Group data of action potential frequencies of CA1 pyramidal neurons in the respective
927 groups ($n_{control}$ = 33 cells, $n_{PLX3397}$ = 30 cells, RM two-way ANOVA followed by Sidak's
928 multiple comparisons).

929 (F) Group data of AMPA receptor-mediated spontaneous excitatory postsynaptic currents
930 (sEPSCs) recorded from CA1 pyramidal neurons revealed no significant changes in excitatory
931 neurotransmission in microglia-depleted tissue cultures ($n_{control}$ = 33 cells, $n_{PLX3397}$ = 30 cells;
932 Mann-Whitney test).

933 Individual data points are indicated by grey dots. Values represent mean ± s.e.m (*** $p < 0.001$;
934 ns, not significant differences).

935 **Figure 5: Dendritic morphology of CA1 pyramidal cells is not affected in microglia-**
936 **depleted tissue cultures**

937 (A) Examples of three dimensionally reconstructed CA1 pyramidal neurons in non-depleted
938 controls and PLX3397 treated, i.e., microglia-depleted tissue cultures. Scale bars, 100 µm.

939 (B) Sholl analysis of apical and basal dendrites from reconstructed CA1 neurons in the
940 respective groups ($n_{control}$ = 20 cells, $n_{PLX3397}$ = 15 cells; RM two-way ANOVA followed by
941 Sidak's multiple comparisons).

942 (C-E) Group data of additional morphological parameters from the same set of reconstructed
943 CA1 pyramidal neurons in microglia-depleted tissue cultures and vehicle-only treated control
944 cultures ($n_{control}$ = 20 cells, $n_{PLX3397}$ = 15 cells; Mann-Whitney test).

945 Individual data points are indicated by grey dots. Values represent mean±s.e.m (ns, not
946 significant differences).

947 **Figure 6: Dendritic spines of CA1 pyramidal neurons are not altered in microglia-**
948 **depleted tissue cultures**

949 (A-C) Examples of dendritic segments and group data of spine densities and spine volumes
950 from patched and posthoc identified CA1 pyramidal neurons in stratum radiatum (rad, A),
951 stratum oriens (sor, B) and stratum lacunosum-moleculare (lcm, C) of PLX3397 treated, i.e.,
952 microglia-depleted tissue cultures and control cultures (rad density: $n_{control}$ = 16 dendritic
953 segments, $n_{PLX3397}$ = 12 dendritic segments; rad volume: $n_{control}$ = 578 spines, $n_{PLX3397}$ = 393
954 spines; oriens density: $n_{control}$ = 15 dendritic segments, $n_{PLX3397}$ = 16 dendritic segments; oriens
955 volume: $n_{control}$ = 450 spines, $n_{PLX3397}$ = 703 spines; lcm density: $n_{control}$ = 36 dendritic segments,
956 $n_{PLX3397}$ = 23 dendritic segments; lcm volume: $n_{control}$ = 655 spines, $n_{PLX3397}$ = 405 spines; Mann-
957 Whitney test). Scale bars, 3 µm.

958 Individual data points are indicated by grey dots. Values represent mean ± s.e.m (ns, not
959 significant differences).

960 **Figure 7: Multi-scale computer modeling of repetitive magnetic stimulation (rMS)**

961 (A) Neuronal responses to rMS were modeled in realistic dendritic morphologies from
962 reconstructed CA1 pyramidal neurons in a stereotypic tissue culture environment. EC,
963 entorhinal cortex; DG, dentate gyrus. Scale bar, 200 µm.

964 (B, C) Changes in membrane voltage (Vm; B) and intracellular calcium levels (Ca^{2+}; C) were
965 assessed for a train of 20 pulses at 10 Hz at the constant stimulation intensity used in the
966 experimental setting. CA1 pyramidal neurons in both conditions showed a delayed
967 suprathreshold response upon repetitive magnetic stimulation.

968 (D) Both the number of cellular spikes upon stimulation and the synaptic weight did not show
969 a significant difference between CA1 pyramidal neurons from microglia-depleted and non-
970 depleted control cultures ($n_{vehicle\text{-}only}$ = 20 cells, $n_{PLX3397}$ = 15 cells; GLMM).

971 (E) In the same set of cells the peak membrane voltage difference in response to magnetic
972 stimulation was modeled in the somatic, apical and basal dendritic compartments. No
973 differences were observed between the two groups, respectively.

974 (F) Analysis of stimulus-triggered changes in intracellular calcium levels. No changes in both
975 the dendritic and the somatic compartments were evident between CA1 pyramidal neurons of
976 microglia-depleted tissue cultures and control cultures.

977 Individual data points are indicated by grey dots. Values represent mean ± s.e.m. (ns, not
978 significant difference).

979 **Figure 8: Repetitive magnetic stimulation (rMS) does not affect microglia morphology**

980 (A-C) Examples of tdTomato expressing microglia in hippocampal area CA1 imaged from
981 *HexB*$^{tdT/tdT}$ cultures over a period of three hours following 10 Hz rMS (2 min intervals).
982 Maximum intensity projections of image-stacks (A), microglial scanning densities (B), and
983 microglial domains (C) are illustrated. Scale bars, 15 µm.

984 (D) Group data of microglial domains and scanning densities from rMS-stimulated and sham-
985 stimulated tissue cultures (n_{sham} = 6 cells, n_{rMS} = 6 cells from 6 cultures in each group; RM two-
986 way ANOVA followed by Sidak's multiple comparisons).

987 Values represent mean ± s.e.m. (ns, not significant difference).

988 **Figure 9: Repetitive magnetic stimulation (rMS) triggers the expression and release of**
989 **plasticity-promoting microglial factors**

990 (A-C) Group data of mRNA and protein levels of (A) tumor necrosis factor alpha (TNFα), (B)
991 interleukin 6 (IL6) and (C) chemokine ligand 1 (CXCL1) in cultures and microglia-depleted
992 cultures (PLX3397 treated cultures) after 10 Hz rMS-stimulated tissue cultures and sham-
993 stimulated controls. ($n_{control}$ = 6 cultures or culturing medium samples respectively for each
994 experimental condition, $n_{PLX3397\ mRNA\ sham}$ = 6 cultures, $n_{PLX3397\ mRNA\ rMS}$ = 7 cultures; $n_{PLX3397}$
995 $_{protein\ levels}$ = 8 culturing medium samples respectively for each experimental condition; Mann-
996 Whitney test, $U_{control\ Tnf\ mRNA}$ = 2, $U_{control\ TNF\ protein}$ = 2, $U_{control\ Il6\ mRNA}$ = 2, $U_{control\ IL6\ protein}$ = 2,
997 $U_{control\ Cxcl1\ mRNA}$ = 3, $U_{control\ CXCL1\ protein}$ = 0).

998 (D) Sample images and group data of eGFP fluorescence intensity of rMS-stimulated and
999 sham-stimulated tissue cultures prepared from TNF-reporter mice [*C57BL/6-Tg(TNFa-eGFP)*]

1000 imaged 3 h after 10 Hz rMS (DG, dentate gyrus; n_{sham} = 26 cultures, n_{rMS} = 27 cultures; Mann-
1001 Whitney test). Scale bars, 200 µm.

1002 Individual data points are indicated by grey dots. Values represent mean ± s.e.m. (* $p < 0.05$,
1003 ** $p < 0.01$; ns, not significant difference).

1004 **Figure 10: Substitution of pro-inflammatory cytokines during stimulation in microglia-**
1005 **depleted tissue cultures rescues rMS-induced synaptic plasticity**

1006 (A) Microglia depleted cultures were stimulated with 10 Hz rMS or sham stimulation. To
1007 simulate the rMS-induced cytokine release on tissue level, the rMS-stimulation of a third set
1008 of cultures was performed in the presence of TNFα (5 ng/ml) and IL6 (2.5 ng/ml).

1009 (B) Group data of AMPA receptor-mediated miniature excitatory postsynaptic currents
1010 (mEPSCs) recorded from CA1 pyramidal neurons in sham-stimulated and 10 Hz rMS-
1011 stimulated cultures (n_{sham} = 51 cells, n_{rMS} = 34 cells, $n_{rMS\text{-}TNF+IL6}$ = 46 cells; Kruskal-Wallis-test
1012 followed by Dunn's post-hoc correction).

1013 Individual data points are indicated by grey dots. Values represent mean ± s.e.m (* $p < 0.05$;
1014 ns, not significant differences).

1015 **Figure 11: Microglia depletion *in vivo* prevents rTMS-induced synaptic plasticity of**
1016 **superficial pyramidal neurons in the medial prefrontal cortex of adult mice**
1017 (A) Post-hoc visualization of superficial pyramidal neurons by streptavidin staining in the
1018 medial prefrontal cortex of adult mice. Microglia was visualized by Iba1 immunolabeling.
1019 Electrophysiological assessment of excitatory synaptic transmission was performed in frontal
1020 sections of non-depleted (left image) and microglia-depleted (BLZ945-treated, right image)
1021 animals. Scale bars, 100 µm.

1022 (B) Quantification of microglial density confirmed a ~90% reduction of microglia in the medial
1023 prefrontal cortex of BLZ945-treated animals ($n_{control}$ = 10 animals, $n_{microglia\text{-}depleted\ (BLZ945)}$ = 5
1024 animals; Mann-Whitney test. U = 0)

1025 (C) 10 Hz repetitive transcranial magnetic stimulation (rTMS) or sham stimulation were
1026 performed in anesthetized adult mice and tissue sections were prepared 2 hours after
1027 stimulation. After slice recovery, excitatory synaptic transmission recordings were performed
1028 3-5 hours post stimulation. In sections from non-depleted animals, a significant increase in the
1029 sEPSC frequency could be detected while die sEPSC amplitude was unchanged. Notably, no
1030 changes in excitatory neurotransmission were detected in microglia-depleted tissue sections
1031 (non-depleted animals: n_{sham} = 89 cells from 6 animals, n_{rTMS} = 81 cells from 6 animals;
1032 microglia-depleted (BLZ945-treated animals): n_{sham} = 48 cells from 2 animals, n_{rTMS} = 51 cells
1033 from 3 animals; Mann-Whitney test. $U_{sEPSC\ frequency,\ non\text{-}depleted}$ = 2324).

1034 (D) sEPSC amplitude-frequency-plots from superficial pyramidal cells in the mPFC of 10 Hz-
1035 rTMS or sham-treated animals (non-depleted or microglia-depleted). While excitatory synaptic
1036 plasticity was evident in non-depleted sections, no changes were detected after microglia-
1037 depletion (RM two-way ANOVA following Sidak's multiple comparisons test).

1038 Individual data points are indicated by grey dots. Values represent mean ± s.e.m (*** $p < 0.001$;
1039 ns, not significant differences).

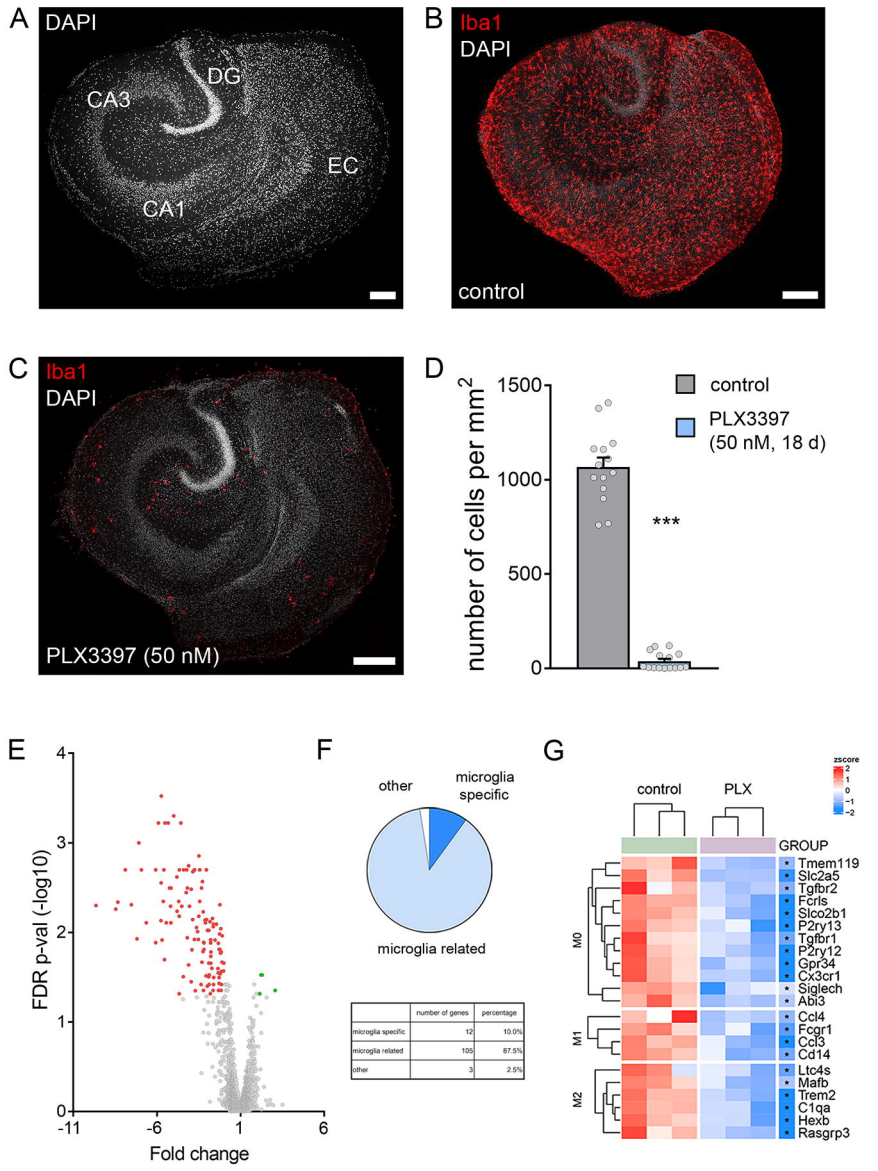
A
DAPI
DG
CA3
EC
CA1
B
Iba1
DAPI
control
C
Iba1
DAPI
PLX3397 (50 nM)
D
number of cells per mm2
1500
1000
500
0
control
PLX3397
(50 nM, 18 d)
***
E
FDR p-val (-log10)
4
3
2
1
0
-11
-6
1
6
Fold change
F
other
microglia
specific
microglia related
number of genes
percentage
microglia specific
12
10.0%
microglia related
105
87.5%
other
3
2.5%
G
control
PLX
zscore
2
1
0
−1
−2
GROUP
M0
M1
M2
Tmem119
Slc2a5
Tgfbr2
Fcrls
Slco2b1
P2ry13
Tgfbr1
P2ry12
Gpr34
Cx3cr1
Siglech
Abi3
Ccl4
Fcgr1
Ccl3
Cd14
Ltc4s
Mafb
Trem2
C1qa
Hexb
Rasgrp3

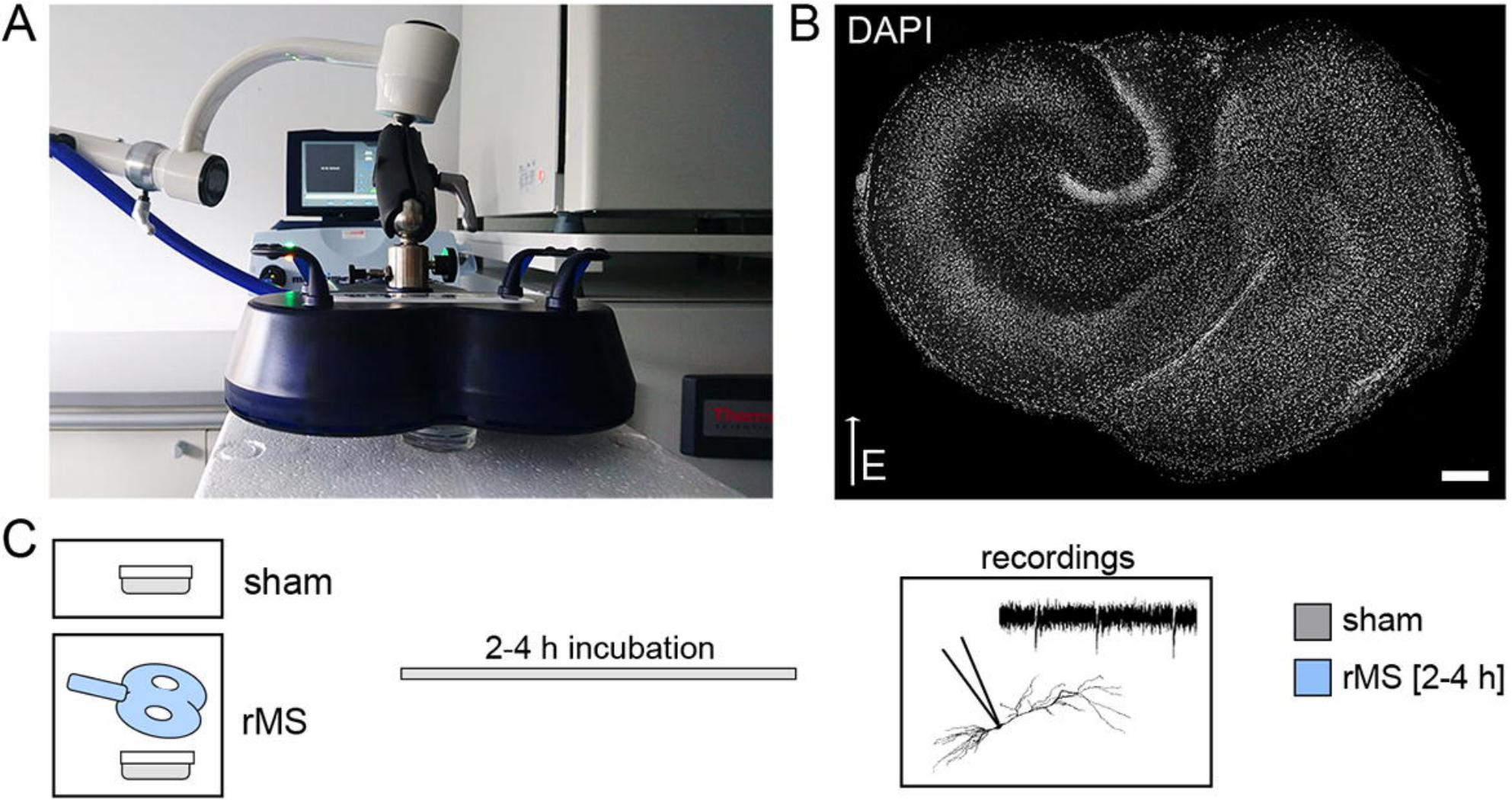
A
B
DAPI
E
C
sham
rMS
2-4 h incubation
recordings
sham
rMS [2-4 h]

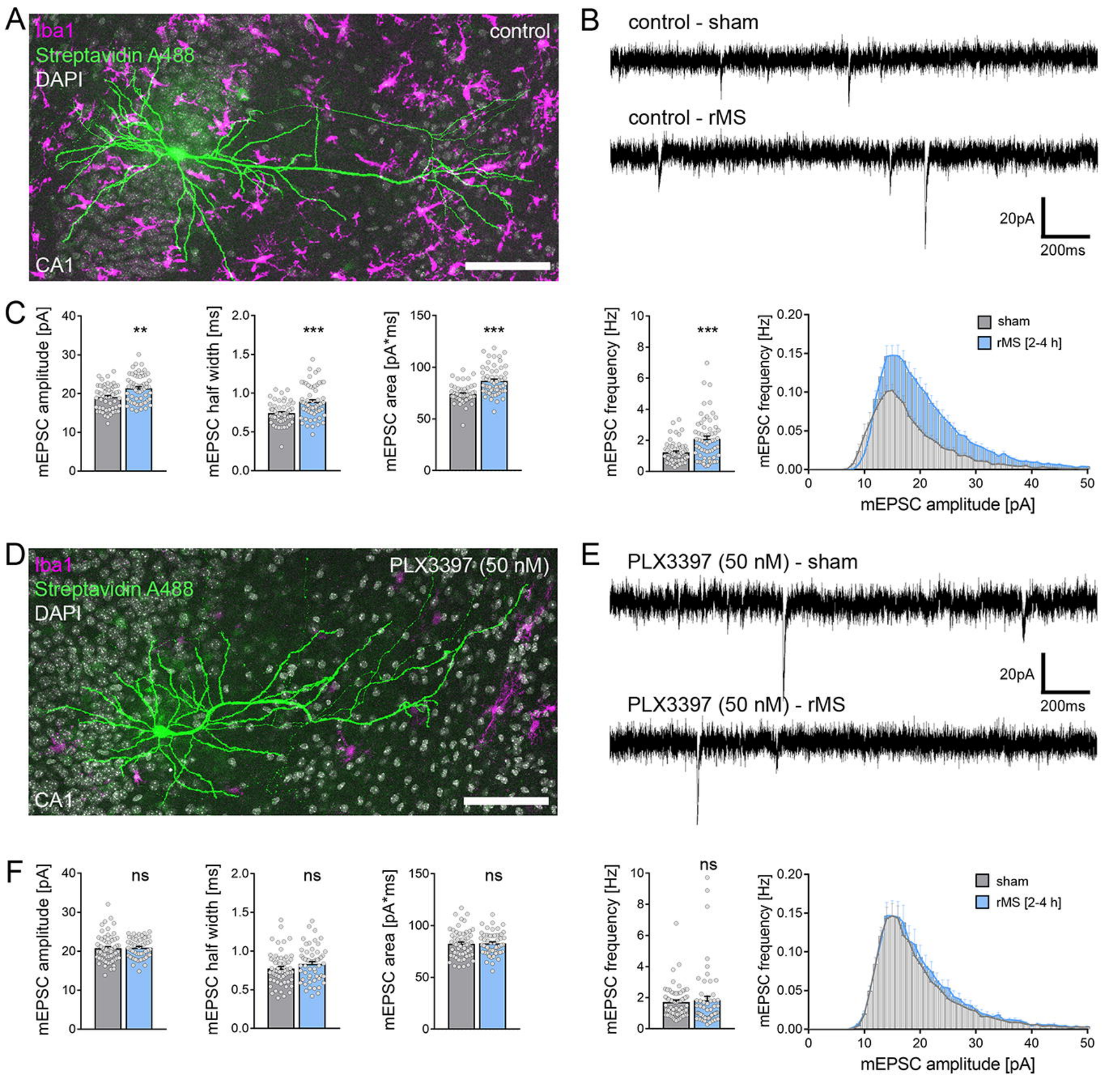
A
Iba1
Streptavidin A488
DAPI
control
CA1
B
control - sham
control - rMS
20pA
200ms
C
mEPSC amplitude [pA]
**
mEPSC half width [ms]
***
mEPSC area [pA*ms]
***
mEPSC frequency [Hz]
***
mEPSC frequency [Hz]
sham
rMS [2-4 h]
mEPSC amplitude [pA]
D
Iba1
Streptavidin A488
DAPI
PLX3397 (50 nM)
CA1
E
PLX3397 (50 nM) - sham
20pA
200ms
PLX3397 (50 nM) - rMS
F
mEPSC amplitude [pA]
ns
mEPSC half width [ms]
ns
mEPSC area [pA*ms]
ns
mEPSC frequency [Hz]
ns
mEPSC frequency [Hz]
sham
rMS [2-4 h]
mEPSC amplitude [pA]

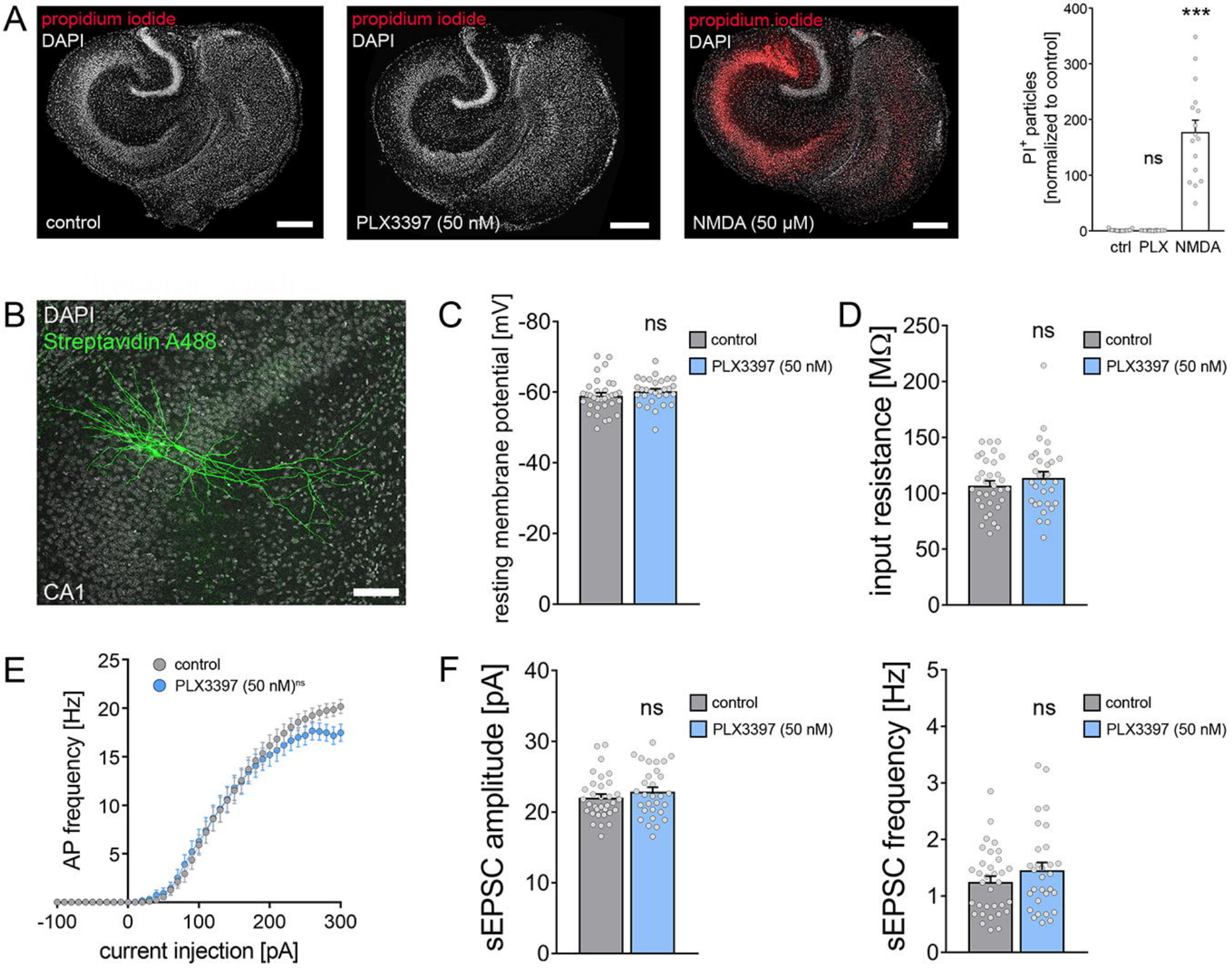
A
propidium iodide
DAPI
control
propidium iodide
DAPI
PLX3397 (50 nM)
propidium iodide
DAPI
NMDA (50 µM)
PI+ particles [normalized to control]
400
300
200
100
0
***
ns
ctrl
PLX
NMDA
B
DAPI
Streptavidin A488
CA1
C
resting membrane potential [mV]
-80
-60
-40
-20
0
ns
control
PLX3397 (50 nM)
D
input resistance [MΩ]
250
200
150
100
50
0
ns
control
PLX3397 (50 nM)
E
AP frequency [Hz]
25
20
15
10
5
control
PLX3397 (50 nM)ns
-100
0
100
200
300
current injection [pA]
F
sEPSC amplitude [pA]
40
30
20
10
0
ns
control
PLX3397 (50 nM)
sEPSC frequency [Hz]
5
4
3
2
1
0
ns
control
PLX3397 (50 nM)

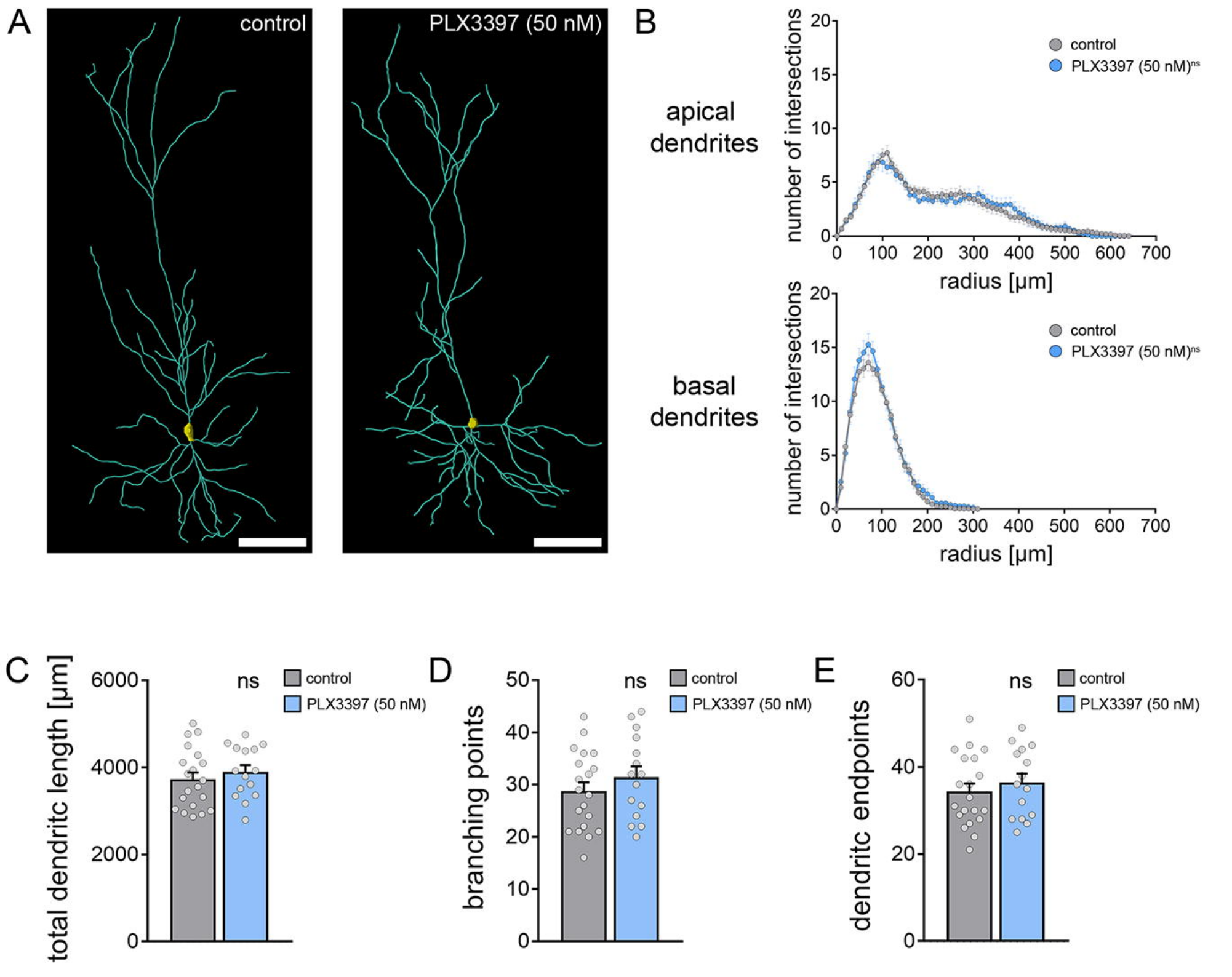
A
control
PLX3397 (50 nM)
B
apical dendrites
basal dendrites
number of intersections
radius [µm]
control
PLX3397 (50 nM)ns
C
total dendritc length [µm]
ns
control
PLX3397 (50 nM)
D
branching points
E
dendritc endpoints

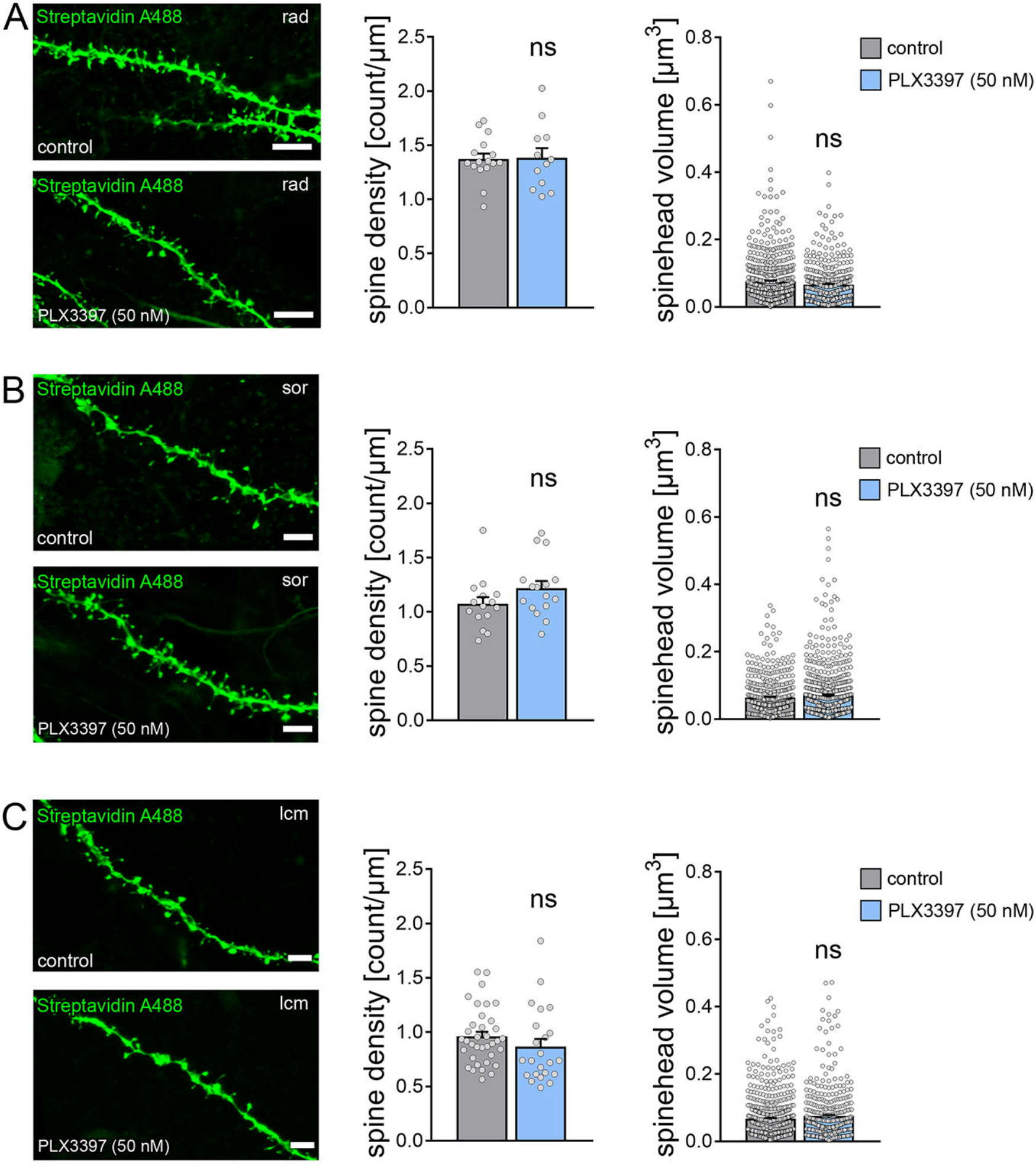
A
Streptavidin A488
rad
control
Streptavidin A488
rad
PLX3397 (50 nM)
spine density [count/µm]
2.5
2.0
1.5
1.0
0.5
0.0
ns
spinehead volume [µm3]
0.8
0.6
0.4
0.2
0.0
ns
control
PLX3397 (50 nM)
B
Streptavidin A488
sor
control
Streptavidin A488
sor
PLX3397 (50 nM)
spine density [count/µm]
ns
spinehead volume [µm3]
ns
control
PLX3397 (50 nM)
C
Streptavidin A488
lcm
control
Streptavidin A488
lcm
PLX3397 (50 nM)
spine density [count/µm]
ns
spinehead volume [µm3]
ns
control
PLX3397 (50 nM)

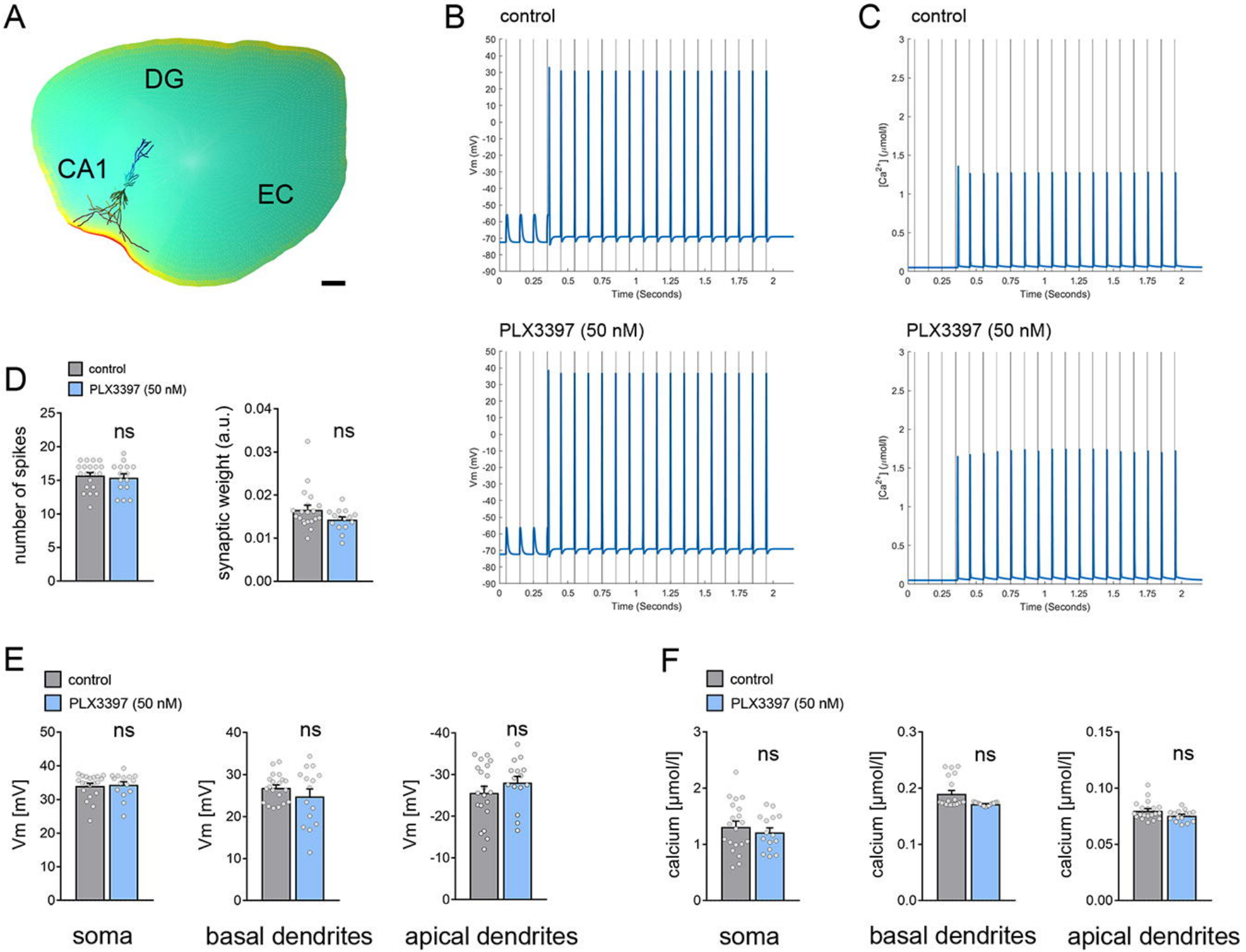
A
DG
CA1
EC
B
control
Vm (mV)
Time (Seconds)
PLX3397 (50 nM)
C
control
[Ca2+] (μmol/l)
Time (Seconds)
PLX3397 (50 nM)
D
control
PLX3397 (50 nM)
number of spikes
ns
synaptic weight (a.u.)
ns
E
control
PLX3397 (50 nM)
Vm [mV]
ns
soma
basal dendrites
apical dendrites
F
control
PLX3397 (50 nM)
calcium [μmol/l]
ns
soma
basal dendrites
apical dendrites

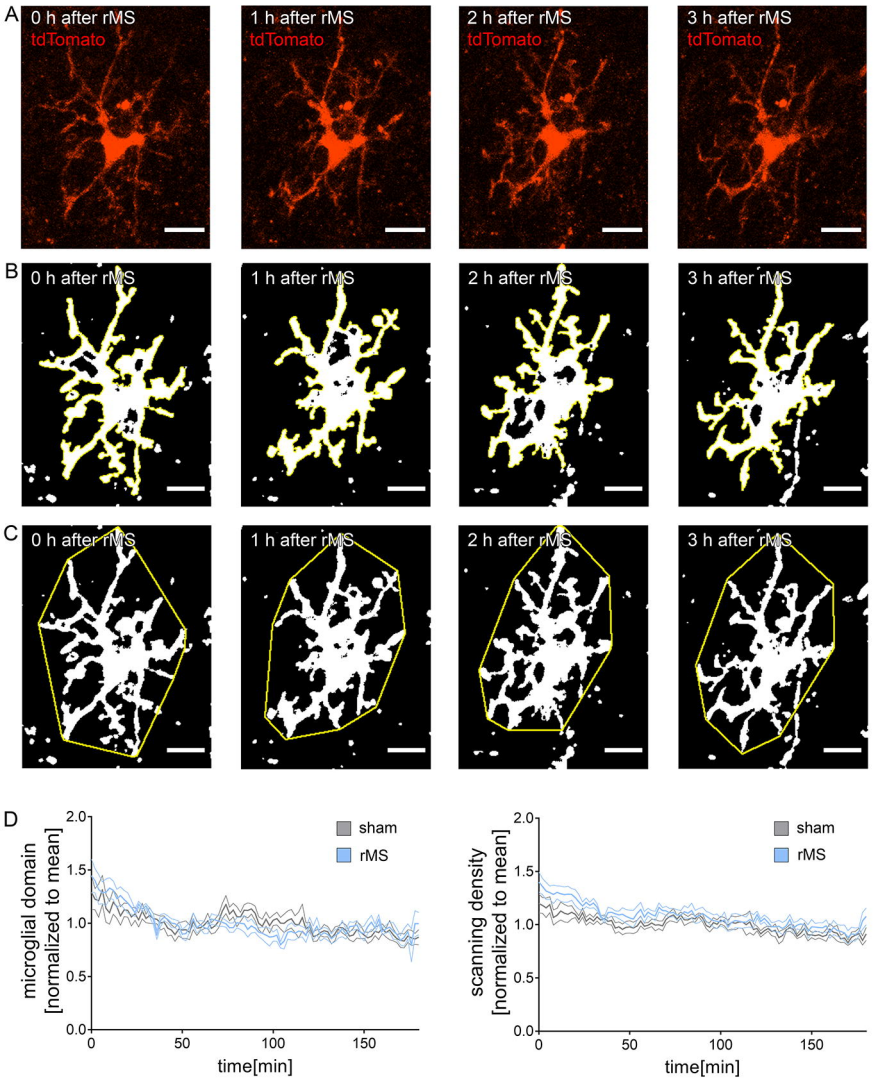
A
0 h after rMS
tdTomato
1 h after rMS
tdTomato
2 h after rMS
tdTomato
3 h after rMS
tdTomato
B
0 h after rMS
1 h after rMS
2 h after rMS
3 h after rMS
C
0 h after rMS
1 h after rMS
2 h after rMS
3 h after rMS
D
microglial domain [normalized to mean]
sham
rMS
2.0
1.5
1.0
0.5
0.0
0
50
100
150
time[min]
scanning density [normalized to mean]
sham
rMS
2.0
1.5
1.0
0.5
0.0
0
50
100
150
time[min]

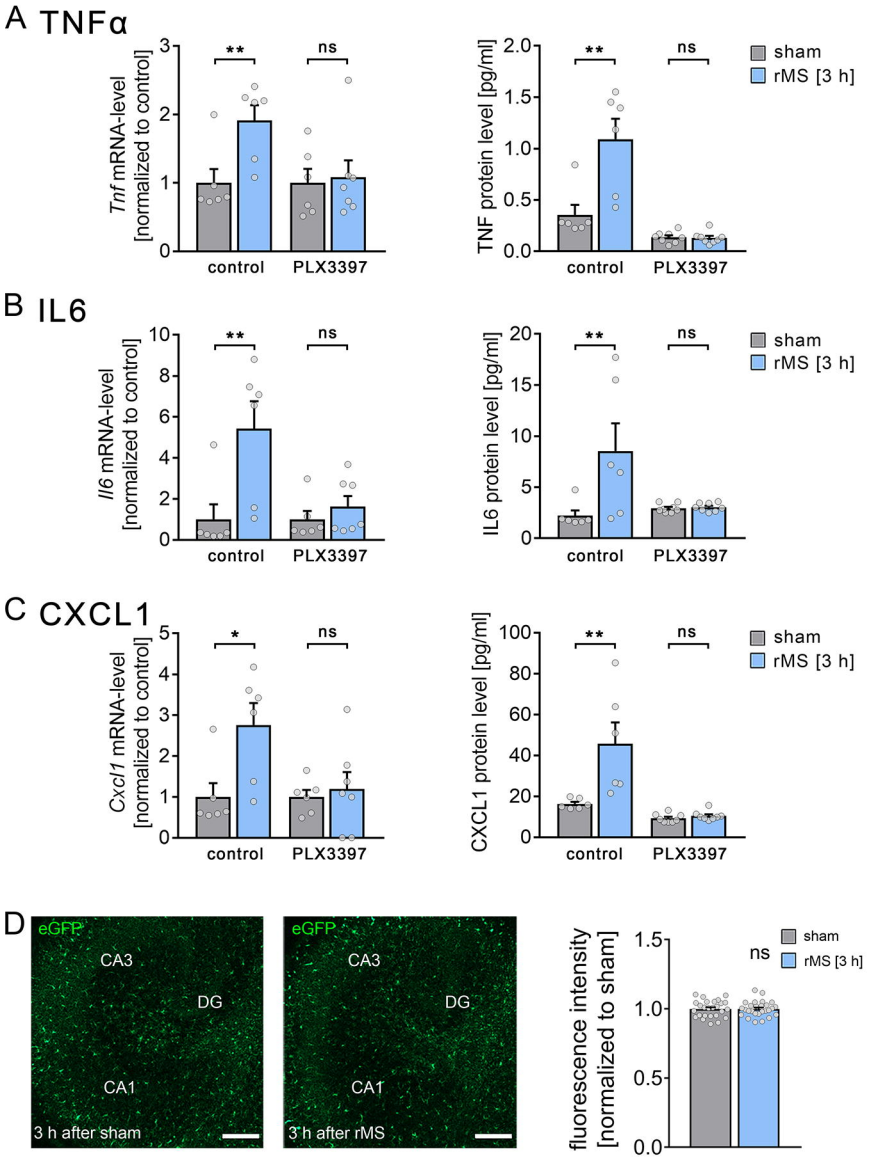
A TNFα
Tnf mRNA-level [normalized to control]
TNF protein level [pg/ml]
sham
rMS [3 h]
control
PLX3397
**
ns
B IL6
Il6 mRNA-level [normalized to control]
IL6 protein level [pg/ml]
C CXCL1
Cxcl1 mRNA-level [normalized to control]
CXCL1 protein level [pg/ml]
*
D
eGFP
CA3
DG
CA1
3 h after sham
3 h after rMS
fluorescence intensity [normalized to sham]

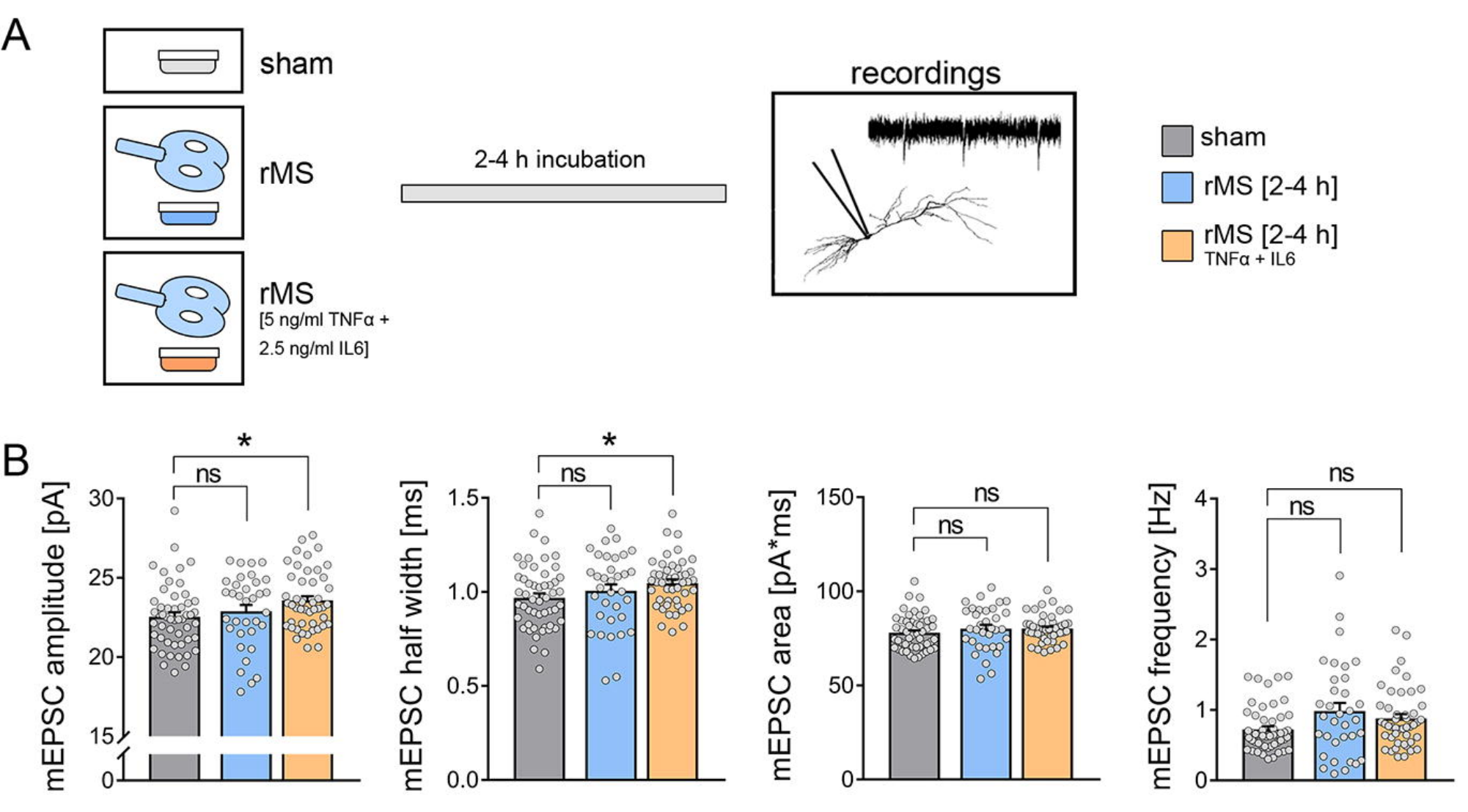
A
sham
rMS
rMS
[5 ng/ml TNFα +
2.5 ng/ml IL6]
2-4 h incubation
recordings
sham
rMS [2-4 h]
rMS [2-4 h]
TNFα + IL6
B
mEPSC amplitude [pA]
mEPSC half width [ms]
mEPSC area [pA*ms]
mEPSC frequency [Hz]
ns
*

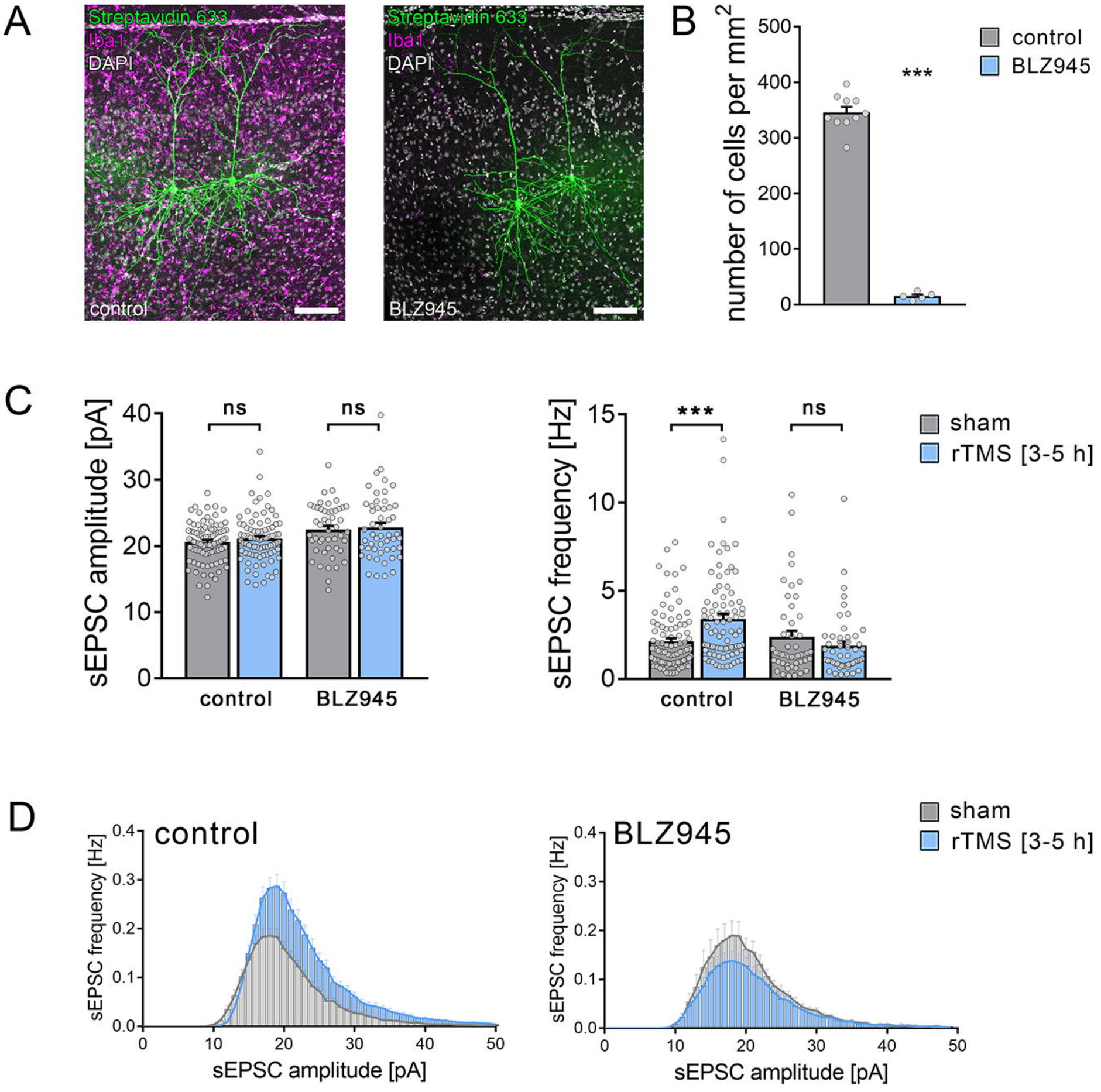
A
Streptavidin 633
Iba1
DAPI
control
Streptavidin 633
Iba1
DAPI
BLZ945
B
number of cells per mm2
500
400
300
200
100
0
***
control
BLZ945
C
sEPSC amplitude [pA]
40
30
20
10
0
ns
ns
control
BLZ945
sEPSC frequency [Hz]
15
10
5
0
***
ns
control
BLZ945
sham
rTMS [3-5 h]
D
control
sEPSC frequency [Hz]
0.4
0.3
0.2
0.1
0.0
0
10
20
30
40
50
sEPSC amplitude [pA]
BLZ945
sham
rTMS [3-5 h]